

# *The imprint of strong-storm tracks on winter weather in North America*

Article

Accepted Version

Lukens, K. E., Berbery, E. H. and Hodges, K. I. ORCID: <https://orcid.org/0000-0003-0894-229X> (2018) The imprint of strong-storm tracks on winter weather in North America. *Journal of Climate*, 31 (5). pp. 2057-2074. ISSN 1520-0442 doi: <https://doi.org/10.1175/jcli-d-17-0420.1> Available at <https://centaur.reading.ac.uk/74401/>

It is advisable to refer to the publisher's version if you intend to cite from the work. See [Guidance on citing](#).

To link to this article DOI: <http://dx.doi.org/10.1175/jcli-d-17-0420.1>

Publisher: American Meteorological Society

All outputs in CentAUR are protected by Intellectual Property Rights law, including copyright law. Copyright and IPR is retained by the creators or other copyright holders. Terms and conditions for use of this material are defined in the [End User Agreement](#).

[www.reading.ac.uk/centaur](http://www.reading.ac.uk/centaur)

**CentAUR**

Central Archive at the University of Reading

Reading's research outputs online





# AMERICAN METEOROLOGICAL SOCIETY

*Journal of Climate*

## **EARLY ONLINE RELEASE**

This is a preliminary PDF of the author-produced manuscript that has been peer-reviewed and accepted for publication. Since it is being posted so soon after acceptance, it has not yet been copyedited, formatted, or processed by AMS Publications. This preliminary version of the manuscript may be downloaded, distributed, and cited, but please be aware that there will be visual differences and possibly some content differences between this version and the final published version.

The DOI for this manuscript is doi: 10.1175/JCLI-D-17-0420.1

The final published version of this manuscript will replace the preliminary version at the above DOI once it is available.

If you would like to cite this EOR in a separate work, please use the following full citation:

Lukens, K., E. Berbery, and K. Hodges, 2017: The Imprint of Strong-Storm Tracks on Winter Weather in North America. *J. Climate*. doi:10.1175/JCLI-D-17-0420.1, in press.

© 2017 American Meteorological Society



# The Imprint of Strong-Storm Tracks on Winter Weather in North America

Katherine E. Lukens

*Department of Atmospheric and Oceanic Science, and Cooperative Institute for Climate and Satellites-Maryland, Earth System Science Interdisciplinary Center, University of Maryland, College Park, College Park, Maryland, USA*

Ernesto Hugo Berbery<sup>1</sup>

*Cooperative Institute for Climate and Satellites-Maryland, Earth System Science Interdisciplinary Center, University of Maryland, College Park, College Park, Maryland, USA*

Kevin I. Hodges

*Department of Meteorology, University of Reading, Reading, United Kingdom*

*Submitted to J. Climate*

21 June 2017

Revised 27 Nov 2017

<sup>1</sup>Corresponding author address: Ernesto Hugo Berbery, 5825 University Research Court, Suite 4001, University of Maryland, College Park, MD, 20740-3823, USA.

<sup>1</sup>Corresponding author email: berbery@umd.edu

1 **Abstract**

2 Northern Hemisphere winter storm tracks and their relation to winter weather are investi-  
3 gated using CFSR data. Storm tracks are described by isentropic PV maxima within a Lagran-  
4 gian framework; these correspond well with those described in previous studies. Our diagnostics  
5 focus on strong-storm tracks, which are comprised of storms that achieve a maximum PV ex-  
6 ceeding the mean value by one standard deviation. Large increases in diabatic heating related to  
7 deep convection occur where the storm tracks are most intense. The cyclogenesis pattern shows  
8 that strong storms generally develop on the upstream sectors of the tracks. Intensification hap-  
9 pens towards the eastern North Pacific and all across the North Atlantic Ocean, where enhanced  
10 storm track-related weather is found.

11 In this study, the relation of storm tracks to near-surface winds and precipitation is evalu-  
12 ated. The largest increases in storm track-related winds are found where strong storms tend to de-  
13 velop and intensify, while storm precipitation is enhanced in areas where the storm tracks have  
14 the highest intensity. Strong storms represent about 16% of all storms but contribute 30-50% of  
15 the storm precipitation in the storm track regions. Both strong-storm related winds and precipita-  
16 tion are prone to cause storm-related losses in the eastern US and North American coasts. Over  
17 the oceans, maritime operations are expected to be most vulnerable to damage offshore of the US  
18 coasts. Despite making up a small fraction of all storms, the strong-storm tracks have a signifi-  
19 cant imprint on winter weather in North America potentially leading to structural and economic  
20 loss.

1 1. INTRODUCTION

2 Two well-documented mid-latitude winter storm tracks in the Northern Hemisphere (NH)  
3 affect North American weather and climate: the Pacific storm track which extends eastward  
4 across the North Pacific Ocean, and the Atlantic storm track which extends northeastward across  
5 the North Atlantic Ocean. Elsewhere in the NH mid-latitudes there is the Mediterranean storm  
6 track which spans eastward across the Mediterranean Sea to the Middle East (Hoskins and  
7 Hodges 2002). The storm tracks are characterized as large narrow bands of high baroclinic insta-  
8 bility along which individual storms tend to propagate, and are maintained by the continuous  
9 downstream development of baroclinic disturbances (Simmons and Hoskins 1979; Wallace et al.  
10 1988; Orlanski and Chang 1993). The upper-tropospheric winds (i.e., the 200-hPa jet stream) and  
11 divergence aloft produce cyclonic circulation poleward of the zonal flow, enhancing cyclonic  
12 shear and generating upstream confluence that can predominantly maintain the mean barocli-  
13 nicity needed for continued downstream eddy activity (Wallace et al. 1988; Hoskins and Valdes  
14 1990). Even in cases of weaker instability, the downstream radiation of kinetic energy in the  
15 form of ageostrophic geopotential fluxes contributes to the growth and intensification of new ed-  
16 dies at the expense of upstream decaying eddies (Simmons and Hoskins 1979; Orlanski and  
17 Chang 1993). Baroclinic disturbances propagate downstream as large-scale wave packets with a  
18 group velocity that primarily dictates the speed at which new eddies develop (Orlanski and  
19 Chang 1993).

20 Many factors influence the NH storm track distribution, including sea surface tempera-  
21 ture (SST) gradients, uneven heating, and orography (Hoskins and Valdes 1990; Held 1993;

22 Brayshaw et al. 2008, 2009; Chang 2009). A strong mid-latitude SST gradient alongside a re-  
23 duced subtropical SST gradient will generally strengthen the storm tracks and shift them pole-  
24 ward (Brayshaw et al. 2008). In the North Atlantic the large SST gradient formed by the protru-  
25 sion of the warm Gulf Stream into the cool higher latitude ocean induces surface wind conver-  
26 gence on the warm side of the Gulf Stream front, intensifying the vertical wind velocity and ver-  
27 tical instability, in turn enhancing convection and storm development (Minobe et al. 2008, 2010).

28         Uneven diabatic heating induced in part by land-sea temperature contrasts plays a role in  
29 storm track modulation (Hoskins and Valdes 1990; Chang 2009). As cool westerly flow off the  
30 land passes over warmer western oceans, the surface air warms rapidly, triggering the generation  
31 of surface sensible heat fluxes that act to destabilize the atmosphere (Mak 1998). The sensible  
32 heat fluxes counter the damping effect of poleward eddy heat fluxes, preserving baroclinicity at  
33 the surface and maintaining the storm tracks through the development of unstable waves aloft  
34 (Hotta and Nakamura 2011). Asymmetries in diabatic heating partly account for the greater  
35 strength of the Atlantic storm track compared to the Pacific storm track, despite the lower baro-  
36 clinicity in the Atlantic (Chang 2009). For instance, the large land-sea temperature gradient in  
37 winter induced by strong air mass contrasts between cold air over northeastern North America  
38 and warmer air over the Gulf Stream form a region of particularly high baroclinic instability  
39 along an axis that follows the North American east coast (Brayshaw et al. 2009). Storms tend to  
40 deepen and intensify leeward of the Appalachian Mountains (Colucci 1976), and the baroclinic  
41 zone over the North American east coast promotes the further amplification of storms, including  
42 nor'easters (Davis and Dolan 1993). Additionally, the strength and areal width of marine storms  
43 are determined by the intensity of the diabatic heating (Mak 1998).

44 As for orographic influences, mountainous terrain mainly acts to suppress storm track ac-  
45 tivity by blocking or deflecting the westerly flow over land (Chang 2009). The Rocky Mountains  
46 deflect westerly Pacific cyclones/storms southward which leads to a southwest-northeast (SW-  
47 NE) tilt in the upper tropospheric jet, the subsequent downstream flow, and the Atlantic storm  
48 track, dynamically separating the Northern Hemisphere storm tracks (Brayshaw et al. 2009;  
49 Chang 2009). The Atlantic track lies coincident with the SW-NE axis of the low-level baroclinic  
50 zone that follows the North American east coast, further enhancing cyclonic activity in the re-  
51 gion of the Atlantic storm track (Brayshaw et al. 2009).

52 During winter, the Pacific and Atlantic storm tracks are collocated with climatological  
53 precipitation maxima that exceed  $6 \text{ mm day}^{-1}$  (Adler et al. 2003; Hawcroft et al. 2015; Xie et al.  
54 2017). Extremely high precipitation is produced primarily by extratropical storms with the most  
55 heavily precipitating storms contributing substantially to the winter climatological precipitation  
56 (Maddox et al. 1979; Hawcroft et al. 2012; Pfahl and Wernli 2012). In general in the NH, over  
57 half of the mean total winter precipitation in the mid-latitudes is associated with frontal systems  
58 and related cyclonic activity (Catto et al. 2012). Specifically in North America, over 70% of win-  
59 ter precipitation is associated with low-level cyclonic activity (Hawcroft et al. 2012). It has also  
60 been found that precipitation and upper-level zonal flow are highly correlated over the mid-lati-  
61 tude oceans and over land upstream of high orography, supporting the notion that strong baro-  
62 clinic cyclones aloft lead to large accumulations of precipitation at the surface (Maddox et al.  
63 1979; Garreaud 2007; Pfahl and Wernli 2012). Accordingly, storm track modulation can be asso-  
64 ciated with changes in the frequency of extreme precipitation and wind events, which can pro-  
65 foundly affect a region's climate (Chang et al. 2002; Ma and Chang 2017). This can happen if a  
66 northward shift and deepening of the semi-permanent Aleutian Low in the high latitudes of the

67 North Pacific Ocean occurs as it can then draw the Pacific storm track poleward and subse-  
68 quently amplify winter precipitation in northwestern North America (Salathé 2006).

69 Previous studies have used different variables and metrics to represent storm tracks, in-  
70 cluding mean sea level pressure (MSLP), geopotential height, and the meridional component of  
71 the upper tropospheric wind (e.g., Gulev et al. 2001; Hoskins and Hodges 2002; Raible 2007).  
72 MSLP and 500-hPa geopotential height are dominated by large scales, making small-scale, high-  
73 frequency features like cyclones difficult to identify without bias toward larger, slower disturb-  
74 ances (Wallace et al. 1988; Hoskins and Hodges 2002). The upper-level meridional wind tends to  
75 better capture the higher frequencies and reveals downstream-developing wave trains along the  
76 storm tracks (Chang and Orlanski 1993; Berbery and Vera 1996). Low-level relative vorticity  
77 and isentropic potential vorticity (PV) are also useful to track storms because of their dependence  
78 on higher order derivatives that allows for the detection of small-scale features such as cyclogen-  
79 esis and cyclolysis (Hoskins and Hodges 2002). PV, in particular, is an ideal dynamical tracer  
80 because of its conservation properties in an adiabatic, frictionless flow (Holton 2004). In the  
81 Northern Hemisphere, a positive (cyclonic) PV anomaly, which generally corresponds to an up-  
82 per-tropospheric pressure trough, induces a vortex with cyclonic circulation (Hoskins et al. 1985;  
83 Hoskins and Hodges 2002). Because PV considers both absolute vorticity and static stability, it  
84 encapsulates many of the dynamic and thermodynamic properties of the atmospheric circulation  
85 while also conforming to the principle of invertibility, which establishes that the 3-dimensional  
86 wind and temperature fields are induced by the PV structure if relatively fast-moving waves are  
87 neglected (Hoskins et al. 1985; Hoskins 1997).

88           This study discusses the characteristics of the storm tracks as constituted by storms that  
89 achieve high potential vorticity and will thus be called “strong-storm tracks”. The primary objec-  
90 tives of the study address the following questions: (1) how do strong-storm tracks relate to sur-  
91 face weather and diabatic heating distributions?, and (2) what are the potential damaging effects  
92 of very high near-surface winds and precipitation rates associated with the strong-storm tracks  
93 that could lead to structural and economic loss in North America? We also discuss the robustness  
94 of the results by using an independent dataset of observed precipitation.

95           The structure of the article is as follows: Section 2 describes the datasets and cyclone  
96 tracking method used. Section 3 discusses the properties of the strong-storm tracks that affect  
97 North America’s winter weather, while Section 4 examines the relation between the strong-storm  
98 tracks and the potential destructive effects of the associated wind and precipitation. Section 5  
99 summarizes the key findings.

100

## 101 2. DATA AND METHODOLOGY

### 102 a. *Datasets*

103           The National Centers for Environmental Prediction (NCEP) Climate Forecast System Re-  
104 analysis (CFSR; Saha et al. 2010) product is the most recent complete compilation of global re-  
105 analysis data generated by NCEP. The CFSR couples the atmosphere, ocean, land surface, and sea  
106 ice to provide our best 4D view of the Earth’s natural state, constrained by observations, every 6  
107 hours. The global atmospheric data have a horizontal grid spacing of 38 km, 64 vertical sigma-  
108 pressure levels and are archived on a  $0.5^\circ \times 0.5^\circ$  latitude-longitude grid. The gridded statistical  
109 interpolation (GSI) scheme assimilates atmospheric variables including global precipitation rates

110 derived from rain gauge and satellite observations into CFSR. The coupled assimilation provides  
111 a more complete and better-quality dataset of precipitation than past NCEP reanalyses that ne-  
112 glect coupling in the data assimilation, with better correspondence between the model physics  
113 and observed precipitation (Saha et al. 2010; Wang et al. 2011). The accuracy of CFSR is im-  
114 proved over past NCEP reanalyses in part because of higher spatial and temporal resolutions, the  
115 assimilation of bias corrected observations, and the coupling to sea ice and the ocean (Saha et al.  
116 2010). Despite the improvements in CFSR, an artificial discontinuity around October 1998 in the  
117 wind and precipitation time series has previously been found. The ingestion of satellite observa-  
118 tions often marks the onset of artificial trends in other reanalysis datasets (Bengtsson et al. 2004),  
119 and CFSR is no different. The discontinuity in CFSR is thought to be due to the introduction of  
120 the assimilation of data from the low-earth polar-orbiting Advanced TIROS Operational Vertical  
121 Sounder (ATOVS) satellite, which contributes to less spin-up of the initial moisture, resulting in  
122 a more humid atmosphere after 1998 (Saha et al. 2010; Chelliah et al. 2011; Wang et al. 2011;  
123 Zhang et al. 2012). Our study uses CFSR data for DJF from 1980-2010 and examines this dis-  
124 continuity to assess the potential effects on our results.

125         The Global Precipitation Climatology Project (GPCP; Huffman et al. 2009) 1-degree  
126 daily dataset of precipitation accumulations centered on 12:00 UTC is used to complement the  
127 reanalysis information. Since October 1996, the GPCP has provided high quality, high resolution  
128 global precipitation data. The daily dataset is derived from the GPCP Version-2 Monthly Precipi-  
129 tation Analysis by combining in situ data (i.e., surface rain gauges) with histograms of 3-hourly  
130 infrared brightness temperatures from geosynchronous-orbit satellite infrared data and precipita-  
131 tion derived from atmospheric parameters retrieved from low earth orbit satellites (Huffman et  
132 al. 2001; Adler et al. 2003; Pendergrass 2015). In this study, GPCP daily precipitation is used for

133 DJF from 1999-2010 and is taken as “ground truth” although some estimates, particularly over  
134 oceans, may be less reliable (Adler et al. 2012).

135

136 *b. Tracking of Storms*

137 Small scale isentropic potential vorticity maxima at the 320 K level (hereafter  $PV_{320}$ ) at  
138 6-hourly intervals are objectively tracked in DJF for 1980-2010 following the Lagrangian ap-  
139 proach discussed in Hoskins and Hodges (2002). The method first identifies cyclones as  $PV_{320}$   
140 anomalies that exceed 0.5 Potential Vorticity Units (PVU, where  $1 \text{ PVU} = 10^{-6} \text{ K m}^2 \text{ kg}^{-1} \text{ s}^{-1}$ ) on  
141 a NH polar stereographic projection, which helps to prevent latitudinal bias in the identification  
142 of cyclones at high latitudes (Sinclair 1997). The  $PV_{320}$  threshold of 0.5 PVU is significantly low  
143 to account for most possible storms: in this case about 296 cyclones per DJF season are identi-  
144 fied that satisfy the post tracking filters (discussed below). The 320 K isentrope is chosen as the  
145 level of analysis as it resides in the mid-upper troposphere near the upper-level jet stream (Fig. 1)  
146 where Rossby wave-induced baroclinic instability tends to occur (Hoskins 1991). The  $PV_{320}$   
147 anomalies are produced by applying a spherical harmonic analysis to the  $PV_{320}$  field and remov-  
148 ing the background planetary scale waves with total wavenumbers less than or equal to 5 and re-  
149 ducing the resolution to T42 to reduce noise. Additionally, a spectral taper is applied to the spec-  
150 tral coefficients to further reduce noise (Hoskins and Hodges 2002). This has been found to be a  
151 conservative but useful approach when examining fields that are dominated by a large scale  
152 background and are very noisy at high resolutions and focuses on the synoptic spatial scales of  
153 cyclones. The identified  $PV_{320}$  maxima are initially linked using a nearest neighbor method to  
154 form tracks and are then refined using a constrained optimization approach which swaps points

155 between tracks to maximize the track smoothness (Hodges 1994, 1995). Constraints are applied  
156 adaptively for maximum propagation speed and track smoothness (Hodges 1999) suitably chosen  
157 for the extra-tropics.

158 Following completion of the tracking, a filter is applied to retain only those cyclones that  
159 last at least 2 days and travel farther than 1000 km. These conditions act as spatial and temporal  
160 filters to remove short duration or semi-stationary eddies. Considering that extratropical storms  
161 at 320 K in the NH have an average  $PV_{\max} = 3$  PVU and a standard deviation  $(PV_{\max})_{SD} = 1.3$   
162 PVU, we define “all-storm tracks” as those shaped by storms with maximum PV that exceed a  
163 low threshold of  $\overline{PV}_{\max} - 1.5 \times (PV_{\max})_{SD} \cong 1$  PVU. As apparent in Fig. 2, this threshold cap-  
164 tures weak cyclogenesis and provides a large number of cases for the analysis: on average, about  
165 259 storms per season that satisfy the post tracking filters comprise the extratropical NH all-  
166 storm tracks.

167 Storms in the Pacific and Atlantic Oceans have an average  $PV_{\max}$  of 3.8 PVU with a  
168 standard deviation of 1 PVU (Both regions have the same values, despite being computed sepa-  
169 rately). “Strong-storm tracks” represent those storms in the Pacific and Atlantic Oceans with  
170 maximum PV that exceeds a higher threshold of  $\overline{PV}_{\max} + 1 \times (PV_{\max})_{SD} = 3.8$  PVU +  
171 1 PVU = 4.8 PVU as also noted in Fig. 2. Strong storms represent about 16% of all storms that  
172 develop in both regions and correspond to similar percentiles of the storm strength distribution in  
173 each basin. On average, 9 (6) strong storms per season develop in the storm track region over the  
174 Pacific (Atlantic) Ocean (Table 1).

175 The statistics of a large number of the cyclone trajectories describe the main properties of  
176 the Northern Hemisphere storm tracks, including the track density, genesis density, lysis density,

177 and mean storm track intensity. Following Hoskins and Hodges (2002), the track density statistic  
178 is calculated by using a single point from each track nearest to each estimation point for each PV  
179 cyclone trajectory; the genesis density statistic uses the first detected positions of the cyclones;  
180 likewise, the lysis density statistic uses the last detected positions of the cyclones, and the spheri-  
181 cal kernel density estimator method (Hodges 1996; Hodges 2008). The genesis and lysis densi-  
182 ties are computed as probability density functions (pdf) and scaled to number densities (per unit  
183 area per month) by multiplying by the number of points and scaling to a unit area equivalent to a  
184  $5^\circ$  spherical cap ( $\sim 10^6 \text{ km}^2$ ); in the case of the track density, the raw statistic is not a pdf but is  
185 scaled to number density by multiplying by the number of tracks and scaled to a unit area equiv-  
186 alent to a  $5^\circ$  spherical cap. The mean intensity statistic is calculated using a kernel regression es-  
187 timator (Hodges 1996) applied to the PV intensity for all points along the cyclone trajectories.  
188 For both the density and regression estimators adaptive smoothing is used (Hodges 1996).

189         Sensitivity tests were carried out to assess the robustness of the results in relation to (a)  
190 the isentropic level of the analysis on which to describe the storm tracks and (b) the PV intensity  
191 threshold, used for the initial identification, above which to consider a cyclone (not shown). An  
192 analysis of storm tracks on different isentropic surfaces (not shown) resulted in the choice of the  
193 320 K isentrope as it is a good intermediate level on which the storm track features are best rep-  
194 resented. The structures and relative intensities of the storm tracks exhibit a lack of sensitivity to  
195 the PV intensity threshold (not shown).

196         In general, the storm tracks and the diabatic heating in the corresponding regions act  
197 symbiotically in that the presence of the heating helps to maintain the baroclinicity needed for  
198 cyclone activity, which in turn influences the 3-dimensional diabatic heating distribution

199 (Hoskins and Valdes 1990). With this co-dependence between the storm tracks and diabatic heat-  
 200 ing in mind, our study explores the direct relationship between the heating and the storm tracks  
 201 that influence North America’s weather. The diabatic heating is computed diagnostically at each  
 202 level between 900 and 100-hPa as the residual in the thermodynamic equation (e.g., Hoskins et  
 203 al. 1989; Barlow et al. 1998; Holton 2004):

$$204 \quad \frac{\dot{Q}(x,y,p,t)}{c_p} = \frac{\partial T}{\partial t} + \mathbf{v} \cdot \nabla T + \omega \left( \frac{\partial T}{\partial p} - \frac{RT}{c_p p} \right), \quad (1)$$

205 where  $\dot{Q}/c_p$  is the residual heating ( $\text{K day}^{-1}$ ),  $T$  the temperature,  $\mathbf{v}$  the horizontal wind vector,  $\omega$   
 206 the vertical wind in pressure coordinates,  $R$  the gas constant for dry air,  $c_p$  the specific heat for  
 207 dry air at constant pressure, and  $p$  the pressure level. The residual is then vertically averaged to  
 208 yield daily diabatic heating estimates of the free atmosphere.

209 To establish the relationship between the storm tracks and diabatic heating, near-surface  
 210 winds, and precipitation, we follow a similar approach to that discussed in Hawcroft et al. (2012)  
 211 and related literature. Each variable is considered to be associated with a cyclone if it is found  
 212 within a particular circular area around the cyclone center. Precipitation from both reanalysis and  
 213 observations is considered to be associated with a storm if it is found within a  $12^\circ$  circular area  
 214 around each storm center, as this is a typical storm precipitation footprint size in the Northern  
 215 Hemisphere winter (Hawcroft et al. 2012). The reanalysis precipitation is associated with storm  
 216 centers identified at corresponding 6-hourly time steps, while the GPCP observations are associ-  
 217 ated with storm center positions at 12:00 UTC each day. Other variables have been reported to  
 218 be greatly affected within the core of a cyclone represented by a  $5^\circ$  cyclone radius (Hawcroft et  
 219 al. 2012, 2015), and this is the choice we consider for diabatic heating and near-surface winds

220 which are associated with the storm centers every 6 hours. The storm-related heating, winds, and  
221 precipitation fields in the figures are masked out at grid points where the average number of  
222 storms is below some very low number (in this case 0.5 storms per unit area per month) in order  
223 to highlight the mid-latitude main activity storm track regions.

224

225 c. *Storm Loss Metrics*

226 To examine the relation between strong-storm tracks and high wind speeds that could  
227 lead to potential damage at the surface, we employ a metric defined by Klawa and Ulbrich  
228 (2003). The metric is represented by a loss index that highlights areas where strong storms are  
229 likely to produce considerable damage by way of winds that exceed the local 98<sup>th</sup> percentile. Fol-  
230 lowing Klawa and Ulbrich (2003),

231 
$$\text{Loss Index} = \sum_{\text{seasons}} N_{\text{pop}} \left( \frac{v}{v_{98}} - 1 \right)^3 \quad \text{for } v \geq v_{98}, \quad (2)$$

232 where  $N_{\text{pop}}$  is the local population number,  $v$  the local wind speed related to the storm  
233 tracks, and  $v_{98}$  the local wind speed at the 98<sup>th</sup> quantile for 1980-2010. Use of this metric has led  
234 to the successful reproduction of storm loss in Germany at the end of the 20<sup>th</sup> century, in turn  
235 leading to a storm loss risk assessment for the nation in the 21<sup>st</sup> century (Klawa and Ulbrich  
236 2003; Donat et al. 2011).

237 Precipitation and storm severity are inherently linked in part by condensational heating  
238 and the enhancement of moisture flux convergence (Trenberth et al. 2003). To our knowledge

239 and unlike for winds, a general relationship between storm track precipitation and damaging ef-  
240 fects has not yet been established. We adopt a simple approach in which we assume that areas  
241 that are most likely to experience loss are those where the storm track precipitation exceeds the  
242 local 98<sup>th</sup> percentile.

243

### 244 3. DYNAMICS OF STORM TRACKS

#### 245 a. *Environment*

246 The Eady Growth Rate, used in this study, combines information of the static stability  
247 and the wind vertical shear for the layer 850-700 hPa, and it is frequently used as a measure of  
248 baroclinic instability (Lindzen and Farrell 1980). Following Hoskins and Valdes (1990), Fig. 3  
249 shows that (1) regions of large baroclinic instability are found over the western Pacific and At-  
250 lantic Oceans (Fig. 3a), and (2) the largest region of low-level baroclinic instability lies poleward  
251 of the 200-hPa jet stream (Fig. 3b). Note that a region of high instability in the western Pacific is  
252 zonal in orientation and parallels the strong 200-hPa jet. In the western Atlantic, the region of  
253 lower troposphere instability also parallels the local upper-level jet maximum with a SW-NE ori-  
254 entation that follows the eastern North American coastline. A secondary region of baroclinic in-  
255 stability is found in the southeast of the Mediterranean Sea and is also poleward of the corre-  
256 sponding local upper-level jet maximum.

257

258 *b. Physical Properties of the Storm Tracks*

259 The characteristics of the 1980-2010 strong winter storm tracks (as stated, those with  
260  $PV_{\max} \geq 4.8$  PVU) are depicted in Fig. 4. In Fig. 4a, the mid-latitude trajectories of individual  
261 strong storms converge into quasi-zonal bands of high cyclonic activity that form the strong-  
262 storm tracks. The number of individual strong storms per unit area, or strong-storm track density  
263 (Fig. 4b), is largest over the Pacific, North American-Atlantic (NAA), and Mediterranean re-  
264 gions. As expected, and in agreement with Wallace et al. (1988) and Hoskins and Valdes (1990),  
265 the three regions of strong-storm tracks are concentrated poleward of the upper-level jets where  
266 there is amplified cyclonic shear and enhanced downstream development of baroclinic disturb-  
267 ances (Figs. 3b, 4b). Fig. 4b also highlights that the strong-storm track density (shades) resem-  
268 bles the track density for all winter storms (as stated, those with  $PV_{\max} \geq 1$  PVU, the threshold  
269 for all-storm tracks, contours), the latter of which is consistent with those presented in Hoskins  
270 and Hodges (2002) and other studies. This is particularly evident over the North Atlantic where  
271 the NAA storm tracks for both strong storms and all storms extend northeastward from central  
272 North America into the higher latitudes near Iceland. The mean intensity statistic denotes the av-  
273 erage strength of the strong-storm tracks identified in DJF (Fig. 4c). The strong-storm tracks are  
274 most intense where the corresponding track densities are highest (i.e., in the eastern North Pa-  
275 cific and western North Atlantic Oceans, and the Mediterranean Sea). The Pacific strong-storm  
276 track intensity (shades) shows an eastward shift relative to the corresponding all-storm track  
277 (contours). The substantial increase in the strength of strong Pacific storms towards the eastern  
278 ocean is indicative of their potential destructive power as they move eastward and hit the North  
279 American west coast. Unlike the Pacific track, the NAA strong-storm track retains its high inten-

280 sity across its respective ocean basin. This suggests that the collocation of the low-level baro-  
281 clinic zone with the highly active NAA strong-storm track helps to invigorate intense storms in  
282 the western Atlantic; in turn, the storms act to reinforce the intensity of the storm track as they  
283 propagate across the ocean.

284 Figs. 4d-e illustrate the general temporal evolution of strong storms (shades) that follow  
285 the storm tracks. The genesis density statistic in Fig. 4d highlights regions of cyclogenesis, i.e.,  
286 the location of the strong storms' initial development. Regions of strong-storm decay are repre-  
287 sented by the lysis density statistic (Fig. 4e). Corresponding characteristics of the all-storm tracks  
288 are also shown by contours in Figs. 4d-e to display the similarity in behavior between the all-  
289 storm and strong-storm tracks.

290 Strong storms that can affect North American weather tend to develop in small groups  
291 near low-level baroclinic zones westward of where the storm tracks peak in intensity (Figs. 3a,  
292 4d). The storms propagate eastward and become strongest over the eastern North Pacific and  
293 western North Atlantic Oceans (Fig. 4c). As they continue to move eastward the strong storms  
294 tend to decay (Fig. 4e), in part as they encounter high orography and become disorganized and  
295 either dissipate or reorganize leeward of the orography and reinvigorate (Fig. 4d-e). Fig. 4d also  
296 shows and supports that strong storms, e.g., intense winter nor'easter storms, which in part are  
297 influenced by heat fluxes over the Gulf Stream, tend to develop over the western North Atlantic  
298 Ocean near the northeastern United States (Kuo et al. 1991; Davis and Dolan 1993; Yao et al.  
299 2008).

300 In the analysis of strong-storm tracks that influence North American weather, it is desira-  
301 ble to take into account the corresponding patterns of diabatic heating for the atmospheric col-  
302 umn. Figs. 5a-c present the diabatic heating climatology, the heating during all storm activity,  
303 and the heating during strong storm activity, respectively. The climatology shows positive heat-  
304 ing rates in the western North Pacific and western North Atlantic Oceans (Fig. 5a), and this pat-  
305 tern resembles the low-level baroclinic instability (Figs. 3a). The distribution of positive heating  
306 rates in the Northern Hemisphere winter is influenced by the distribution of the warm Kuroshio  
307 and Gulf Stream currents in the western North Pacific and North Atlantic Oceans, respectively,  
308 and by the zonal asymmetry of the land-ocean distribution (Brown 1964; Geller and Avery 1978;  
309 Wei et al. 1983). In contrast to the climatology, the heating during all storm activity increases in  
310 strength and spreads across the North Pacific and North Atlantic Oceans in the mid-latitudes  
311 (Fig. 5b). The heating is even more intense during strong storm activity (Fig. 5c). In the North  
312 Pacific, the heating further intensifies in the east where the Pacific strong-storm track is most in-  
313 tense, and it remains strong as it spreads up and down the west coast of North America. In rela-  
314 tion to the NAA strong-storm track, the heating is most intense over the western North Atlantic  
315 and remains strong across the ocean where the storm track retains its high intensity.

316 Fig. 5d presents the ratio of the positive heating rates related to strong-storm activity to  
317 the positive heating rates related to all-storm activity. This comparison between the strong-storm  
318 and all-storm heating reveals that the heating related to the strong-storm tracks is at least 25%  
319 more intense than the heating related to the all-storm tracks over the Pacific and Atlantic Oceans  
320 where the storm tracks are strongest. Moreover, in the lower mid-latitudes, the strong-storm heat-  
321 ing is up to 3 times more intense than the all-storm heating.

322 Deep convection associated with strong-storm activity is obtained directly as a diagnostic  
323 from the CFSR database (Fig. 6). High positive heating rates associated with deep convection are  
324 found in each of the strong-storm track regions and are highest where the storm tracks are most  
325 intense (see Figs. 4b-c). Furthermore, the heating from deep convection largely resembles the di-  
326 abatic heating distribution in the strong-storm track regions (Figs. 5c), suggesting that deep con-  
327 vective processes dominate the strong-storm tracks in the free atmosphere.

328 The strong-storm diabatic heating in the western North Atlantic corresponds with the  
329 higher track density and is more intense than the heating in the North Pacific (Figs. 4b, 5c). Simi-  
330 lar relationships are found in the deep convection associated with strong-storm tracks (Fig. 6).  
331 Along with the local SW-NE oriented low-level baroclinic zone and upper-level jet near the east  
332 coast of North America (Fig. 3), the stronger heating in the Atlantic promotes greater instability  
333 and increased cyclonic activity (Fig. 4b), supporting the findings of Brayshaw et al. (2009).

334

#### 335 4. RELATION OF STORM TRACKS TO SURFACE WEATHER

336 The near-surface wind distribution can change dramatically during the evolution of in-  
337 tense extratropical cyclones, and this is cause for concern for two reasons. First, in populated  
338 areas there is great potential for the wind to inflict serious damage and put lives in jeopardy, and  
339 second, over open waters strong near-surface winds have great impacts where maritime transpor-  
340 tation, fishing vessels, and manned offshore oil and gas production units are most vulnerable  
341 (Bell et al. 2017). Strong storms can also change the winter precipitation distribution by generat-  
342 ing excessive amounts in a relatively short amount of time (days to a week). Lasting and possibly

343 devastating effects like major flooding and wind damage may result leading to states of emer-  
344 gency, especially when the cumulative impacts and insurance losses from several storms occur-  
345 ring in rapid succession are considered (Mailier et al. 2006). The patterns of intense near-surface  
346 winds and heavy precipitation rates in strong-storm tracks over North America are explored next.

347

#### 348 *a. Near-surface Winds*

349 The relation between the storm tracks and near surface winds will be discussed next with  
350 the support of Figs. 7 and 8. In the absence of storm activity (Fig. 7a), near-surface winds  
351 achieve magnitudes of about  $4\text{-}6\text{ m s}^{-1}$  and resemble the pattern of the upper-level jet presented  
352 in Fig. 3b with primarily eastward and northeastward directions in the North Pacific and North  
353 Atlantic Oceans, respectively. Fig. 7b shows that for both the Pacific and NAA all-storm tracks  
354 (i.e., storms with  $PV_{\max} \geq 1\text{ PVU}$ ), the near-surface winds intensify where the storm tracks are  
355 strongest and shift eastward in the eastern ocean basins. The winds associated with the strong-  
356 storm tracks (i.e.,  $PV_{\max} \geq 4.8\text{ PVU}$ ) presented in Fig. 7c show further intensification and a  
357 stronger eastward shift over the oceans.

358 The increases in wind speed related to the all-storm tracks are better seen in Figs. 8a and  
359 8b that depict the difference and ratio, respectively, between the all-storm related wind speeds  
360 and the no-storm wind speeds. Likewise, Figs. 8c and 8d depict the wind speed difference and  
361 ratio between strong-storm and no-storm events. In the North Pacific Ocean, wind speeds in-  
362 crease in the eastern basin where the all-storm track is strongest (Fig. 8a), particularly in the  
363 lower and higher mid-latitudes where they are over 5 times more intense (Fig. 8b). The winds  
364 over the ocean further intensify during strong storm activity (Figs. 8c-d), helping to drive strong

365 storms eastward to the North American coast. Moving to the Atlantic sector, wind speeds are  
366 found to intensify across the North Atlantic but particularly in the west and lower mid-latitudes  
367 with a secondary maximum towards the northeastern sector (Figs. 8a-b; also seen in Fig 7c).  
368 During strong storm activity, wind speeds are further enhanced, specifically in the west just off-  
369 shore of North America (Figs. 8c-d). Over land, near-surface wind speeds related to the all-storm  
370 tracks increase east of the Rocky Mountains (Figs. 8a-b). Greater intensification in the wind  
371 speeds is evident during strong-storm events (Figs. 8c-d), specifically in the eastern US where  
372 the corresponding strong-storm track strengthens (see Fig. 4c).

373 Overall the strong-storm tracks leave greater imprints in the near-surface wind field in the  
374 North Atlantic than in the North Pacific (Fig. 7c), most notably just offshore of North America  
375 where maritime shipping and oil platforms are exposed. Increases in wind speeds near the coasts  
376 are also more pronounced in the western North Atlantic (Figs. 8c-d), consistent with the distribu-  
377 tions of diabatic heating and deep convection that indicate greater baroclinic instability in the re-  
378 gion (see Figs. 5c, 6). This would suggest that maritime operations in the western North Atlantic  
379 are more at risk to damage by way of near-surface winds associated with the strong-storm tracks.

380 The potential damage associated with extratropical strong-storm tracks over land in North  
381 America is assessed taking into account very high near-surface storm wind speeds, i.e., those that  
382 exceed the local 98<sup>th</sup> percentile (Fig. 9). Areas east of high orography experience the highest per-  
383 cent of strong-storm days with near-surface wind speeds above the 98<sup>th</sup> percentile (Fig. 9a). As  
384 seen in Fig. 9b, these same areas also experience the most intense wind speeds related to the  
385 strong-storm tracks.

386 Intense near-surface winds do not necessarily imply damage, unless they occur over pop-  
387 ulated areas. Fig. 9c presents the 2010 population number obtained from the LandScan Global  
388 Population Project following the methodology in Dobson et al. (2000), which is used for the cal-  
389 culation of the storm loss index presented in section 2c. The storm loss estimate (Fig. 9d) high-  
390 lights the regions that are most vulnerable to damages from very high storm winds. Within North  
391 America, these areas are in the eastern US spanning from the Midwest to the east coast states, as  
392 well as along the southwestern US coast. A comparison with Fig. 9a reveals that storm wind loss  
393 in these areas is associated with up to 16% of strong storms in winter.

394

#### 395 *b. Precipitation*

396 Figure 10 presents the relation between the storm tracks and surface precipitation. Figs.  
397 10a and 10b show the precipitation distributions related to all-storm tracks and to strong-storm  
398 tracks, respectively. Consistent with the findings in Hawcroft et al. (2012), the all-storm and  
399 strong-storm precipitation maxima are found in the North Pacific and North Atlantic Oceans as  
400 well as along the west coast of North America. Secondary precipitation maxima are found in the  
401 southeastern United States. Overall the storm tracks leave greater imprints in the precipitation in  
402 the North Atlantic than in the North Pacific, possibly associated with the warmer waters that fa-  
403 vor increased baroclinic instability and deep convection (see Figs. 3a, 6).

404 The difference and ratio between the strong-storm and all-storm track precipitation (Figs.  
405 10c and 10d respectively) indicate the noticeable increases in precipitation that result from the  
406 fewer but stronger storms. These increases are evident over the oceans where the storm tracks are  
407 most intense. The percent contribution of strong-storm precipitation to the all-storm precipitation

408 (Fig. 10e) shows that strong storms represent about 16% of all storms, yet they contribute 30-  
409 50% of the precipitation associated with the Pacific and NAA storm tracks (discussed further be-  
410 low).

411 As expected, precipitation associated with strong-storm activity in the eastern Pacific  
412 Ocean is more intense than that associated with all-storm activity (Figs. 10a-c). Towards the US  
413 west coast, precipitation increases during strong-storm activity (Figs. 10c-d) and contributes to  
414 almost half of the all-storm precipitation in the region (Fig. 10e), exposing local fishing and  
415 other maritime operations to potential damage. Further increases are found as North America's  
416 land contrasts and orographic effects come into play: in the western US, increases of 50% are  
417 found during strong storm activity (Figs. 10d-e). This supports the notion that cyclones aloft lead  
418 to large accumulations of precipitation upstream of great mountain ranges and other high orogra-  
419 phy (Garreaud 2007). Farther east, strong-storm tracks are also associated with more intense pre-  
420 cipitation rates (Fig. 10c-d), contributing to over 30% of the all-storm precipitation (Fig. 10e).  
421 Orography in the northeastern United States can further boost the precipitation from strong  
422 storms. Similar results are found in the western North Atlantic where the enhanced strong-storm  
423 precipitation contributes to 30% of the all-storm precipitation (Figs. 10c-e).

424 The susceptibility to damage from heavy precipitation, i.e., precipitation rates exceeding  
425 the local 98<sup>th</sup> percentile, during strong storm activity is investigated for North America (Fig. 11).  
426 The percent of strong-storm days with precipitation rates exceeding the local 98<sup>th</sup> percentile is  
427 presented in Fig. 11a. Distributions of heavy precipitation related to the all-storm and strong-  
428 storm tracks are shown in Figs. 11b and 11c, respectively. The heaviest precipitation related to  
429 the all-storm and strong-storm tracks is found along the west coast and in the southeastern US

430 (Figs. 11b-c). The strong-storm tracks in particular likely play key roles in shaping the precipita-  
431 tion distribution in the southeastern US as the region experiences a relatively high percentage of  
432 strong-storm days with precipitation exceeding the 98<sup>th</sup> percentile (Fig. 11a). Along the west  
433 coast where there are fewer strong-storm days with heavy precipitation, it is likely that in addi-  
434 tion to the strong-storm tracks, other factors such as topography and land-ocean contrasts may  
435 influence the distribution of heavy precipitation. In the central US, the high percentage of strong-  
436 storm days with heavy precipitation corresponds to low strong-storm precipitation rates (Figs.  
437 11a,c). This indicates that in winter the region is relatively dry during strong-storm activity and  
438 is therefore less likely to experience loss associated with precipitation exceeding the 98<sup>th</sup> percen-  
439 tile.

440 Fig. 11d highlights the differences between the heavy strong-storm and all-storm track  
441 precipitation, and Fig. 11e presents the percent contribution of strong storms to all-storm precipi-  
442 tation that exceeds the 98<sup>th</sup> percentile. Substantial increases in precipitation rates during strong  
443 storm activity are found in the southeastern US and near the US east coast (Fig. 11d). Areas with  
444 the largest increases in heavy precipitation correspond to regions where strong storms contribute  
445 well over 30% of the all-storm precipitation (Fig. 11e), indicating their vulnerability to damage  
446 related to heavy strong-storm precipitation. The southeastern US is particularly vulnerable as  
447 precipitation is greatly enhanced during strong storm activity and contributes almost 50% of  
448 heavy all-storm precipitation in the region.

449

450 c. *Reanalysis vs. observed precipitation related to the Storm Tracks*

451           The precipitation blending algorithm in CFSR combines pentad Climate Prediction Cen-  
452 ter (CPC) Merged Analysis of Precipitation (CMAP) and daily gauge precipitation analyses of  
453 varying spatial resolutions with background 6-hourly precipitation from the Global Data Assimi-  
454 lation System, GDAS (Saha et al. 2010). The blending algorithm in CFSR is latitude dependent:  
455 in the tropics it tends to the CMAP analysis, in the mid-latitudes to a gauge analysis, and in the  
456 high latitudes to the model precipitation. Therefore, despite CFSR including precipitation in its  
457 assimilation cycle, deviations from observations may occur. During 1999-2010, daily GPCP pre-  
458 cipitation rates are considerably less intense than the daily reanalysis precipitation rates (not  
459 shown, but almost identical to the 1980-2010 reanalysis precipitation rates), particularly north of  
460 60°N along the southern coastlines of Alaska and Greenland. As stated, this and other differences  
461 in winter precipitation between CFSR and GPCP may be due to multiple reasons, including the  
462 precipitation blending algorithm in CFSR but also inadequate satellite-driven estimations of pre-  
463 cipitation at high latitudes included in the daily GPCP dataset (Bolvin et al. 2009).

464           We examine whether the relation of the strong-storm tracks with the daily reanalysis pre-  
465 cipitation is maintained over North America when using precipitation derived from observations,  
466 that is, the daily precipitation from GPCP (section 2). To this end, and despite that GPCP became  
467 available in 1996, the period 1999-2010 is examined to avoid any eventual spurious effects due  
468 to the 1998 discontinuity found in CFSR. The 1999-2010 daily precipitation distributions associ-  
469 ated with the all-storm and strong-storm tracks for GPCP are shown in Figs. 12a and 12b, respec-  
470 tively. Comparison with the reanalysis precipitation (Figs. 10a-b) indicates that they share simi-  
471 lar spatial distributions with local maxima over the eastern North Pacific Ocean, the western  
472 North Atlantic Ocean, the west coast of North America, and the southeastern United States. Nev-  
473 ertheless, the GPCP precipitation does exhibit weaker intensities, particularly in the Pacific and

474 NAA storm track regions over the oceans. It is likely that the discrepancy in magnitude results  
475 from uncertainties in the oceanic observations of precipitation described in Adler et al. (2012).

476         Similar inferences can be noted in the difference (Fig. 12c) and ratio (Fig. 12d) of the ob-  
477 served precipitation related to the all-storm and strong-storm tracks. Differences in the reanalysis  
478 and observed precipitation metrics are noted particularly in the western North Atlantic Ocean  
479 where the observed precipitation related to the strong-storm tracks is shown to decrease (Fig.  
480 12c). As already stated, the uncertainties in oceanic observations may play a role in this discrep-  
481 ancy. Over land, the observed precipitation differences and ratios in Figs. 12c and 12d show in-  
482 creases along the US west coast and in the southeastern US, consistent with the reanalysis (see  
483 Figs. 10c-d). The contribution of strong storms to the observed all-storm precipitation is pre-  
484 sented in Fig. 12e. As depicted in the reanalysis (Fig. 10e), observations show that strong storms  
485 contribute over 30% of the all-storm precipitation over land and the oceans.

486         We also analyze the relation of the storm tracks with precipitation from GPCP that ex-  
487 ceeds the local 98<sup>th</sup> percentile in North America (Fig. 13). Comparison of the reanalysis (Figs.  
488 11b-e) and observational metrics reveal similarities despite the weaker GPCP intensities. The in-  
489 tense precipitation observed over the continent (Figs. 13a-b) corresponds qualitatively well with  
490 the reanalysis, in particular in the eastern US and along the North American west coast where the  
491 precipitation is further enhanced during strong storm activity (Fig. 13c). According to Fig. 13d,  
492 strong storms contribute over 30% of the all-storm precipitation that exceeds the 98<sup>th</sup> percentile  
493 in regions where large increases are observed. The results indicate that the eastern US and the  
494 west coast of North America are most prone to damage from heavy strong-storm precipitation,

495 consistent with the findings using CFSR (section 4b). In general, we find that the reanalysis pre-  
496 cipitation distributions related to the all-storm and strong-storm tracks are consistent with obser-  
497 vations.

498

499 *d. The 1998 CFSR data discontinuity and the Storm Tracks*

500 It was earlier stated that the reanalysis data show a discontinuity in the wind and precipi-  
501 tation fields in October 1998 thought to be due to the ingestion of data from ATOVS at the time.  
502 For instance, after 1998 there is a marked decrease in the intensity of low-level winds in the trop-  
503 ics and an increase in the global average precipitation (Chelliah et al. 2011; Wang et al. 2011).  
504 We investigate what impact, if any, this jump has on the results. To this end, the subset periods  
505 of 1980-1998 (hereafter, the early period) and 1999-2010 (hereafter, the later period) are ana-  
506 lyzed. Table 1 displays relevant strong-storm statistics for the early and later periods to assess  
507 any change in the strong winter storm tracks that could impact the North American climate. The  
508 statistics are normalized to units per season and include the number of strong storms identified,  
509 the mean intensity of the strong storms, and the average maximum intensity reached by the  
510 strong storms during each period. Furthermore, each decade between 1980 and 2010 is examined  
511 to explore the possibility of a trend in the storm tracks regardless of the discontinuity.

512 The more important feature noted in Table 1a is that no noticeable variations are found in  
513 the statistical means between the early and later periods and among the decades within 1980-  
514 2010. This indicates that the CFSR discontinuity does not significantly influence NH storm track

515 behavior. Further, the effect of the discontinuity on the Pacific and NAA strong-storm tracks sep-  
516 arately is investigated (Tables 1b-c), and it is found again that the behavior of each of the storm  
517 tracks is unaffected.

518 A related evaluation was performed for the relation between the strong-storm tracks and  
519 the near-surface wind and precipitation distributions (not shown). Again, it was found that the  
520 1998 CFSR discontinuity has little or no influence on the results corresponding to North Ameri-  
521 can high impact weather. The wind speed associated with strong-storm tracks in each of these  
522 periods resembles that for the entire period and the same is true for the strong-storm precipita-  
523 tion. In summary, it is found that the CFSR discontinuity does not affect any of the features dis-  
524 cussed in this article.

525

## 526 5. CONCLUDING REMARKS

527 The behavior of strong winter storm tracks and their imprint on storm track-related  
528 weather in North America are discussed using 31 years of data from the Climate Forecast System  
529 Reanalysis and 12 years of precipitation data from the Global Precipitation Climatology Project.  
530 It is found that a data discontinuity in October 1998 in CFSR does not affect the behavior of the  
531 Northern Hemisphere storm tracks, nor does it influence their relation with North American win-  
532 ter weather. Storms are defined as maxima in potential vorticity and objectively tracked through  
533 their lifecycles following a Lagrangian approach. Two types of storm tracks are discussed: the  
534 first one, “all-storm tracks”, includes all extratropical cyclones whose maximum PV intensities  
535 exceed a low threshold of 1 PVU; the second type, “strong-storm tracks”, only includes storms  
536 that achieve a maximum potential vorticity of at least 4.8 PVU, which is the value exceeding the

537 mean intensity of storms comprising the Pacific and NAA storm tracks by one standard devia-  
538 tion. These more intense extratropical cyclones make up about 16% of all winter storms. Both  
539 all-storm tracks and strong-storm tracks are found to correspond well with those described in  
540 previous studies: over the North Pacific Ocean and over the North Atlantic Ocean (as well as a  
541 weaker one over the Mediterranean Sea). In addition to detecting larger structures like the mean  
542 intensity of the storm tracks, and because of the dependence of PV on higher order derivatives,  
543 small-scale features of the storm tracks are easily differentiated, i.e., regions of cyclogenesis and  
544 cyclolysis. The cyclogenesis pattern shows that strong storms generally develop near low-level  
545 baroclinic zones. The cyclolysis pattern reveals that the strong storms tend to dissipate in the  
546 eastern North Pacific Ocean, the western North Atlantic Ocean near eastern Canada, and a sec-  
547 ondary area over the central United States. The symbiotic relation between storm tracks and dia-  
548 batic heating is evidenced in the large increases in diabatic heating associated with deep convec-  
549 tive processes. The heating increases occur where the strong-storm tracks are most intense, in  
550 particular over the oceans.

551         The analysis of the relation of strong-storm tracks to the near-surface wind distribution  
552 indicates that the winds shift eastward during strong storm activity. Furthermore, the wind  
553 speeds increase over the oceans where the storm tracks are most intense, i.e., in the eastern North  
554 Pacific and western North Atlantic Oceans. Over North America, areas east of the Rockies ex-  
555 hibit large increases in wind speed during strong storm activity. It is found that the precipitation  
556 associated with strong-storm tracks is most intense where they are strongest. Moreover, the pre-  
557 cipitation during strong storm activity is more intense than that during all storm activity, espe-  
558 cially in the North Atlantic Ocean where the NAA storm track density is particularly high. While

559 strong-storms make up about 16% of all-storms, they contribute 30-50% of the all-storm precipi-  
560 tation over the oceans and over North America. Calculations based on an observed precipitation  
561 dataset (GPCP) confirm results based only on CFSR products and thus support the robustness of  
562 the findings.

563         The analysis of very high wind speeds and heavy precipitation related to the strong-storm  
564 tracks provides an inference of their destructive potential in North America. While the most in-  
565 tense strong-storm wind speeds are found in the central United States, areas most likely to expe-  
566 rience the greatest storm wind-related loss span from the Midwest to the east coast states as well  
567 as along the southwestern US coast. Heavy precipitation is further enhanced during strong storm  
568 activity, with the largest increases occurring along the west coast, in the southeastern US, and  
569 near the US east coast. In these areas, strong storms contribute over 30% of the all-storm precipi-  
570 tation that exceeds the local 98<sup>th</sup> percentile, indicating their vulnerability to damages from heavy  
571 precipitation during strong storm activity.

572         Our findings indicate that strong-storm tracks leave a significant imprint on winter  
573 weather in North America, despite making up a small fraction of all storms that develop. This  
574 imprint depends not only on dynamical features but also on the density of the population, thus  
575 showing the greatest loss in the eastern US and North American coasts. Over the water, it would  
576 be expected that oil platforms and maritime shipping and fishing craft are most vulnerable to  
577 storm-related damages just offshore of the US coasts.

578

579 *Acknowledgements*

580           The authors are thankful to the anonymous reviewers for their suggestions and comments  
581 that significantly improved the article. We also acknowledge Matthew Hawcroft for computa-  
582 tional support, and Alfredo Ruiz-Barradas, Ryan Smith, Patrick Meyers, Michael Peterson, and  
583 Stephen Doore for their helpful suggestions. This study was supported by NOAA grant  
584 NA14NES4320003.

585           The storm trajectories used in this study have been made freely available online in ASCII  
586 form on the Cooperative Institute for Climate and Satellites-Maryland (CICS-MD) website,  
587 <http://cicsmd.umd.edu/data-downloads/data-sets/>

588

589

590

591 **References**

- 592 Adler, R.F., G.J. Huffman, A. Chang, R. Ferraro, P. Xie, J. Janowiak, B. Rudolf, U. Schneider,  
593 S. Curtis, D. Bolvin, A. Gruber, J. Susskind, P. Arkin, E. Nelkin 2003: The Version 2  
594 Global Precipitation Climatology Project (GPCP) Monthly Precipitation Analysis (1979-  
595 Present). *J. Hydrometeor.*, **4**, 1147-1167.
- 596 Adler, R. F., G. Gu, and G. J. Huffman, 2012: Estimating Climatological Bias Errors for the  
597 Global Precipitation Climatology Project (GPCP). *J. Appl. Meteor. Climatol.*, **51**, 84-99,  
598 doi: 10.1175/JAMC-D-11-052.1.
- 599 Barlow, M., S. Nigam, and E. H. Berbery 1998: Evolution of the North American Monsoon Sys-  
600 tem. *J. Climate*, **11**, 2238-2257.
- 601 Bell, R. J., S. L. Gray, and O. P. Jones, 2017: North Atlantic storm driving of extreme wave  
602 heights in the North Sea. *J. Geophys. Res. Oceans*, **122**, 3253-3268, doi:  
603 10.1002/2016JC012501.
- 604 Bengtsson, L., S. Hagermann, and K. I. Hodges, 2004: Can climate trends be calculated from re-  
605 analysis data? *J. Geophys. Res.*, **109**, D11111, doi: 10.1029/2004JD004536.
- 606 Berbery, E. H., and C. S. Vera, 1996: Characteristics of the Southern Hemisphere winter storm  
607 track with filtered and unfiltered data. *J. Atmos. Sci.*, **53**, 468-481.
- 608 Bolvin, D. T., R. F. Adler, G. J. Huffman, E. J. Nelkin, and J. P. Poutiainen, 2009: Comparison  
609 of GPCP Monthly and Daily Precipitation Estimates with High-Latitude Gauge Observa-  
610 tions. *J. Applied Meteor. Clim.*, **48**, 1843-1857, doi: 10.1175/2009JAMC2147.1.
- 611 Brayshaw, D. J., B. Hoskins, and M. Blackburn, 2008: The storm-track response to idealized  
612 SST perturbations in an aquaplanet GCM. *J. Atmos. Sci.*, **65**, 2842-2860.

613 Brayshaw, D. J., B. Hoskins, and M. Blackburn, 2009: The basic ingredients of the North Atlan-  
614 tic storm track. Part I: Land-sea contrast and orography. *J. Atmos. Sci.*, **66**, 2539-2558,  
615 doi: 10.1175/2009JAS3078.1.

616 Brown, Jr., J. A., 1964: A diagnostic study of tropospheric diabatic heating and the generation of  
617 available potential energy. *Tellus*, 16:3, 371-388, doi: 10.3402/tellusa.v16i3.8931.

618 Catto, J. L., C. Jakob, G. Berry, and N. Nicholls, 2012: Relating global precipitation to atmos-  
619 pheric fronts. *Geophys. Res. Lett.*, **39**, L10805, doi: 10.1029/2012GL051736.

620 Chang, E. K. M., and I. Orlanski, 1993: On the dynamics of a storm track. *J. Atmos. Sci.*, **50**,  
621 2038-2053.

622 Chang, E. K. M., S. Lee, and K. L. Swanson, 2002: Storm track dynamics. *J. Climate*, **15**, 2163-  
623 2183.

624 Chang, E. K. M., 2009: Diabatic and orographic forcing of northern winter stationary waves and  
625 storm tracks. *J. Climate*, **22**, 670-688, doi: 10.1175/2008JCLI2403.1.

626 Chelliah, M., W. Ebisuzaki, S. Weaver, and A. Kumar, 2011: Evaluating the tropospheric varia-  
627 bility in National Centers for Environmental Prediction's climate forecast system reanaly-  
628 sis. *J. Geophys. Res.*, **116**, D17107.

629 Colucci, S. J., 1976: Winter cyclone frequencies over the eastern United States and adjacent  
630 western Atlantic. *Bull. Amer. Meteor. Soc.*, **57(5)**, 548-553.

631 Davis, R. E., and R. Dolan, 1993: Nor'easters. *American Scientist*, **81**, 428-439.

632 Dobson, J. E., E. A. Bright, P. R. Coleman, R. C. Durfee, B. A. Worley, 2000: A Global Popula-  
633 tion database for Estimating Populations at Risk. *Photogrammetric Engineering & Re-*  
634 *mote Sensing*, **66**, 849-857.

635 Donat, M. G., G. C. Leckebusch, S. Wild, and U. Ulbrich, 2011: Future changes in European  
636 winter storm losses and extreme wind speeds inferred from GCM and RCM multi-model  
637 simulations. *Nat. Hazards Earth Syst. Sci.*, **11**, 1351-1370, [https://doi.org/10.5194/nhess-](https://doi.org/10.5194/nhess-11-1351-2011)  
638 [11-1351-2011](https://doi.org/10.5194/nhess-11-1351-2011).

639 Garreaud, R., 2007: Precipitation and circulation covariability in the extratropics. *J. Climate*, **20**,  
640 4789-4797, doi: 10.1175/JCLI4257.1.

641 Geller, M. A., and S. K. Avery, 1978: Northern Hemisphere distributions of diabatic heating in  
642 the troposphere derived from general circulation data. *Mon. Wea. Rev.*, **106**, 629-636.

643 Gulev, S. K., O. Zolina, and S. Grigoriev, 2001: Extratropical cyclone variability in the Northern  
644 Hemisphere winter from the NCEP/NCAR reanalysis data. *Clim. Dyn.*, **17**, 795-809.

645 Hawcroft, M. K., L. C. Shaffrey, K. I. Hodges, and H. F. Dacre, 2012: How much Northern  
646 Hemisphere precipitation is associated with extratropical cyclones? *Geophys. Res. Lett.*,  
647 **39**, L24809.

648 Hawcroft, M. K., L. C. Shaffrey, K. I., Hodges, and H. F. Dacre, 2015: Can climate models rep-  
649 resent the precipitation associated with extratropical cyclones? *Clim. Dyn.*, 1-17, doi:  
650 [10.1007/s00382-015-2863-z](https://doi.org/10.1007/s00382-015-2863-z).

651 Held, I. M., 1993: Large-Scale Dynamics and Global Warming. *Bull. Amer. Meteor. Soc.*, **74**,  
652 228-241.

653 Hodges, K. I., 1994: A general method for tracking analysis and its application to meteorological  
654 data. *Mon. Wea. Rev.*, **122**, 2573-2586.

655 Hodges, K. I., 1995: Feature tracking on the unit sphere. *Mon. Wea. Rev.*, **123**, 3458-3465.

656 Hodges, K. I., 1996: Spherical Nonparametric Estimators Applied to the UGAMP Model Inte-  
657 gration for AMIP. *Mon. Wea. Rev.*, **124**, 2914-2932.

658 Hodges, K. I., 1999: Adaptive constraints for feature tracking. *Mon. Wea. Rev.*, **127**, 1362-1373.

659 Hodges, K. I., 2008: Confidence Intervals and Significance Tests for Spherical Data Derived  
660 from Feature Tracking. *Mon. Wea. Rev.*, **136**, 1758-1777, doi:  
661 10.1175/2007MWR2299.1.

662 Holton, J. R., 2004: An introduction to dynamic meteorology, 4<sup>th</sup> edition. *Intl Geophys. Series*,  
663 **88**.

664 Hoskins, B. J., M. E. McIntyre, and A. W. Robertson, 1985: On the use and significance of isen-  
665 tropic potential vorticity maps. *Quart. J. Roy. Meteor. Soc.*, **111**, 877-946.

666 Hoskins, B. J., and P. J. Valdes, 1990: On the existence of storm-tracks. *J. Atmos. Sci.*, **47**, 1854-  
667 1864.

668 Hoskins, B. J., 1991: Towards a PV- $\theta$  view of the general circulation. *Tellus*, **43**, 27-35.

669 Hoskins, B. J., 1997: A potential vorticity view of synoptic development. *Meteorol. Appl.*, **4**,  
670 325-334.

671 Hoskins, B. J., and K. I. Hodges, 2002: New perspectives on the Northern Hemisphere  
672 winter storm tracks. *J. Atmos. Sci.*, **59**, 1041-1061.

673 Hoskins, B. J., H. H. Hsu, I. N. James, M. Masutani, P. D. Sardeshmukh, and G. H. White, 1989:  
674 Diagnostics of the global atmospheric circulation based on ECMWF analyses 1979-  
675 1989. WMO/TD-No. 326, World Meteorological Organization, 217 pp.

676 Hotta, D., and H. Nakamura, 2011: On the significance of the sensible heat supply from the  
677 ocean in the maintenance of the mean baroclinicity along storm tracks. *J. Climate*, **24**,  
678 3377-3401, doi: 10.1175/2010JCLI3910.1.

679 Huffman, G.J., R.F. Adler, M. Morrissey, D.T. Bolvin, S. Curtis, R. Joyce, B McGavock, J.  
680 Susskind, 2001: Global Precipitation at One-Degree Daily Resolution from Multi-Satel-  
681 lite Observations. *J. Hydrometeor.*, **2**, 36-50.

682 Huffman, G. J., R. F. Adler, D. T. Bolvin, and G. Gu, 2009: Improving the Global Precipitation  
683 Record: GPCP Version 2.1. *Geophys. Res. Lett.*, **36**, L17808, doi:  
684 10.1029/2009GL040000.

685 Klawa, M., and U. Ulbrich, 2003: A model for the estimation of storm losses and the identifica-  
686 tion of severe winter storms in Germany. *Nat. Hazards Earth Syst. Sci.*, **3**, 725–732, doi:  
687 10.5194/nhess-3-725-2003.

688 Kuo, Y.-H., R. J. Reed, and S. Low-Nam, 1991: Effects of surface energy fluxes during the early  
689 development and rapid intensification states of seven explosive cyclones in the western  
690 Atlantic. *Mon. Wea. Rev.*, **119**, 457-476.

691 Lindzen, R. S., and B. Farrell, 1980: A simple approximate result for maximum growth rate of  
692 baroclinic instabilities. *J. Atmos. Sci.*, **37**, 1648-1654.

693 Ma, C.-G., and E. K. M. Chang, 2017: Impacts of storm-track variations on wintertime extreme  
694 weather events over the continental United States. *J. Climate*, **30**, 4601-4624, doi:  
695 10.1175/JCLI-D-16-0560.1.

696 Maddox, R. A., C. F. Chappell, and L. R. Hoxit, 1979: Synoptic and meso-scale aspects of flash  
697 flood events. *Bull. Amer. Meteor. Soc.*, **60**, 115-123, doi:10.1175/1520-0477-60.2.115.

698 Mailier, P. J., D. B. Stephenson, C. A. T. Ferro, and K. I. Hodges, 2006: Serial clustering of ex-  
699 tratropical cyclones. *Mon. Wea. Rev.*, **134**, 2224-2240.

700 Mak, M., 1998: Influence of surface sensible heat flux on incipient marine cyclogenesis. *J. At-*  
701 *mos. Sci.*, **55**, 820-834.

702 Minobe, S., A. Kuwano-Yoshida, N. Komori, S.-P. Xie, and R. J. Small, 2008: Influence of the  
703 Gulf Stream on the troposphere. *Nature*, **452(7184)**, 206-209, doi: 10.1038/nature06690.

704 Minobe, S., M. Miyashita, A. Kuwano-Yoshida, H. Tokinaga, and S.-P. Xie, 2010: Atmospheric  
705 response to the Gulf Stream: seasonal variations. *J. Climate*, **23**, 3699-3719, doi:  
706 10.1175/2010JCLI3359.1.

707 Orlandi, I., and E. K. M. Chang, 1993: Ageostrophic geopotential fluxes in downstream and up-  
708 stream development of baroclinic waves. *J. Atmos. Sci.*, **50**, 212-225.

709 Pendergrass, A., and NCAR Staff (Eds), 2015: The Climate Data Guide: GPCP (Daily): Global  
710 Precipitation Climatology Project. Retrieved from  
711 [https://climatedataguide.ucar.edu/climate-data/gpcp-daily-global-precipitation-climatol-](https://climatedataguide.ucar.edu/climate-data/gpcp-daily-global-precipitation-climatol-ogy-project)  
712 [ogy-project](https://climatedataguide.ucar.edu/climate-data/gpcp-daily-global-precipitation-climatol-ogy-project)

713 Pfahl, S., and H. Wernli, 2012: Quantifying the relevance of cyclones for precipitation extremes.  
714 *J. Climate*, **25**, 6770-6780, doi: 10.1175/JCLI-D-11-00705.1.

715 Raible, C. C., 2007: On the relation between extremes of midlatitude cyclones and the atmos-  
716 pheric circulation using ERA40. *Geophys. Res. Lett.*, **34**, L07703, doi:  
717 10.1029/2006GL029084.

718 Saha, S., and coauthors, 2010: The NCEP Climate Forecast System Reanalysis. *Bull. Amer. Me-*  
719 *teor. Soc.*, **91**, 1015-1057, doi: 10.1175/2010BAMS3001.1.

720 Salathé, E. P., Jr., 2006: Influences of a shift in North Pacific storm tracks on western North  
721 American precipitation under global warming. *Geophys. Res. Lett.*, **33**, L19820.

722 Simmons, A. J., and B. J. Hoskins, 1979: The downstream and upstream development of unsta-  
723 ble baroclinic waves. *J. Atmos. Sci.*, **36**, 1239-1254.

724 Sinclair, M. R., 1997: Objective identification of cyclones and their circulation intensity, and cli-  
725 matology. *Weather and Forecasting*, **12**, 595-612.

726 Trenberth, K. E., A. Dai, R. M. Rasmussen, and D. B. Parsons, 2003: The changing character of  
727 precipitation. *BAMS*, **84**, 1205-1217, doi: 10.1175/BAMS-84-9-1205.

728 Wallace, J. M., G.-H. Lim, and M. L. Blackmon, 1988: Relationship between cyclone tracks, an-  
729 ticyclone tracks and baroclinic waveguides. *J. Atmos. Sci.*, **45**, 439-462.

730 Wang, W., P. Xie, S. H. Yoo, Y. Xue, A. Kumar, and X. Wu, 2011: An assessment of the surface  
731 climate in the NCEP climate forecast system reanalysis, *Clim. Dynamics*, **37**, 1601-1620,  
732 doi: 10.1007/s00382-010-0935-7.

733 Wei, M-Y, D. R. Johnson, and R. D. Townsend, 1983: Seasonal distributions of diabatic heating  
734 during the First GARP Global Experiment. *Tellus*, **35A**, 241-255.

735 Xie, P., R. Joyce, S. Wu, S. Yoo, Y. Yarosh, F. Sun, and R. Lin, 2017: Reprocessed, Bias-Cor-  
736 rected CMORPH Global High-Resolution Precipitation Estimates from 1998. *J. Hydro-*  
737 *meteor.* doi:10.1175/JHM-D-16-0168.1, in press.

738 Yao, Y., W. Perrie, W. Zhang, and J. Jiang, 2008: Characteristics of atmosphere-ocean interac-  
739 tions along North Atlantic extratropical storm tracks. *J. Geophys. Res.*, **113**, D14124, doi:  
740 10.1029/2007JD008854.

741 Zhang, L., A. Kumar, and W. Wang, 2012: Influence of changes in observations on precipitation:  
742 a case study for the Climate Forecast System Reanalysis (CFSR), *J. Geophys. Res.*, **117**,  
743 D08105, doi:10.1029/2011JD017347.

744 **Table**

745

<b>(a) Northern Hemisphere</b>	<b>1980-2010</b>	<b>1980-1998</b>	<b>1999-2010</b>	<b>1981-1990</b>	<b>1991-2000</b>	<b>2001-2010</b>
<i>Number of Strong Storms (season<sup>-1</sup>)</i>	26	24	29	26	24	30
<i>Mean Intensity (PVU)</i>	3.8	3.8	3.8	3.8	3.8	3.8
<i>Average Max Intensity (PVU)</i>	5.4	5.4	5.4	5.4	5.4	5.4

<b>(b) Pacific storm track</b>	<b>1980-2010</b>	<b>1980-1998</b>	<b>1999-2010</b>	<b>1981-1990</b>	<b>1991-2000</b>	<b>2001-2010</b>
<i>Number of Strong Storms (season<sup>-1</sup>)</i>	9	9	9	10	7	9
<i>Mean Intensity (PVU)</i>	3.8	3.8	3.8	3.8	3.7	3.8
<i>Average Max Intensity (PVU)</i>	5.3	5.3	5.3	5.3	5.3	5.3

<b>(c) North American-Atlantic storm track</b>	<b>1980-2010</b>	<b>1980-1998</b>	<b>1999-2010</b>	<b>1981-1990</b>	<b>1991-2000</b>	<b>2001-2010</b>
<i>Number of Strong Storms (season<sup>-1</sup>)</i>	6	5	8	5	6	8
<i>Mean Intensity (PVU)</i>	3.8	3.8	3.8	3.8	3.8	3.9
<i>Average Max Intensity (PVU)</i>	5.3	5.3	5.3	5.3	5.3	5.3

746

747

748

749

750 **Table 1:** Statistics for the DJF strong-storm tracks for (a) the entire Northern Hemisphere, (b) the Pacific storm track, and (c) the  
751 North American-Atlantic storm track. In (b) and (c), only strong storms that develop within the specified storm track domain are in-  
752 cluded. The first column shows the values for the entire 31-year period. The following two columns denote the early and later periods.  
753 The last three columns highlight the values for each decade.

754 **Figure Caption List**

755 Figure 1: DJF mean zonal state in the Northern Hemisphere for 1980-2010. The mean zonal  
756 wind is shaded with  $5.0 \text{ m s}^{-1}$  intervals. Line contours indicate the vertical distribution of  
757 mean zonal isentropic surfaces at a  $10 \text{ K}$  contour interval. The bold black line highlights  
758 the  $\theta=320\text{K}$  surface on which the mid-latitude storm tracks are defined.

759 Figure 2: Histogram of all DJF storms binned by maximum intensity in the Northern Hemisphere  
760 for 1980-2010. Maximum intensity bins are shown in the x-direction at an interval of  $0.2$   
761 PVU. Storms included in the all-storm track analysis have maximum intensities of  $1$  PVU  
762 or greater. Strong storms that follow the Pacific (PAC) or North American-Atlantic  
763 (NAA) storm tracks have maximum intensities of  $4.8$  PVU or greater and are highlighted  
764 in warm colors. In parentheses in the labels, NH signifies the statistics for the Northern  
765 Hemisphere, while ST indicates the statistics for the PAC and NAA storm tracks.

766 Figure 3: (a) 1980-2010 DJF Eady growth rate average for the  $850\text{-}700 \text{ hPa}$  layer. Values ex-  
767 ceeding  $0.2 \text{ day}^{-1}$  are shaded at  $0.2 \text{ day}^{-1}$  intervals. Masked areas over the continents indi-  
768 cate regions where the land extends above the  $850\text{-hPa}$  surface. (b) Zonal mean wind at  
769  $200\text{-hPa}$ . Values exceeding  $15 \text{ m s}^{-1}$  are shaded.

770 Figure 4: Storm track statistics in the Northern Hemisphere DJF season for 1980-2010. All-storm  
771 tracks properties are depicted in contours, while the strong-storm track properties are  
772 shaded. (a) Individual trajectories of strong storms; (b) Track density for all-storm tracks  
773 (contours at intervals of  $3.0$  storms per  $10\text{e}6 \text{ km}^2$  per month) and strong-storm tracks  
774 (shaded at intervals of  $0.5$  storms per  $10\text{e}6 \text{ km}^2$  per month); (c) Mean intensity of all-  
775 storm tracks (contour intervals of  $0.4$  PVU) and strong-storm tracks (shaded at intervals  
776 of  $0.2$  PVU); (d) cyclogenesis density for all-storm tracks (contours at intervals of  $0.4$

777 storms per  $10^6 \text{ km}^2$  per month) and strong-storm tracks (shaded at intervals of 0.05  
778 storms per  $10^6 \text{ km}^2$  per month); (e) as (d) but for cyclolysis.

779 Figure 5: DJF 1980-2010 vertically averaged 900-100 hPa diabatic heating: (a) Climatology; (b)  
780 during all storm activity; and (c) during strong storm activity. (d) The ratio (%) of the  
781 strong-storm diabatic heating to the all-storm diabatic heating. Shaded regions in (d) indi-  
782 cate areas where the all-storm and strong-storm heating rates are positive.

783 Figure 6: Mean heating from deep convection during strong storm activity averaged between  
784 900-100 hPa in the Northern Hemisphere DJF season for 1980-2010. Contour interval is  
785  $1.0 \text{ K day}^{-1}$ . Regions outside the all-storm track regions are masked out.

786 Figure 7: Mean near-surface wind distributions on the hybrid level 1 in DJF for 1980-2010 (a)  
787 during no storm activity, (b) during all storm activity, and (c) during strong storm activ-  
788 ity. Shaded intervals are  $2.0 \text{ m s}^{-1}$ . In (b) and (c), regions outside the all-storm track re-  
789 gions are masked out.

790 Figure 8: Wind speed comparisons based on Fig. 7. (a) Difference between all-storm wind speed  
791 and no-storm wind speed. (b) Ratio (%) of the all-storm wind speed to the no-storm wind  
792 speed. (c) Difference between strong-storm wind speed and no-storm wind speed. (d) Ra-  
793 tio (%) of strong-storm wind speed to the no-storm wind speed. In (a) and (c), shaded in-  
794 tervals are  $1.0 \text{ m s}^{-1}$ . In (b) and (d), values exceeding 100% are shaded with intervals of  
795 50%. Regions outside the all-storm track regions are masked out.

796 Figure 9: Analysis of intense near-surface wind speeds in DJF for 1980-2010 in North America.  
797 (a) Percent of strong-storm days with wind speeds exceeding the local 98<sup>th</sup> percentile.  
798 Shaded intervals are 2%. (b) Mean strong-storm wind speeds exceeding the local 98<sup>th</sup>  
799 percentile. Shaded intervals are  $2 \text{ m s}^{-1}$ . (c) 2010 population number with an interval of

800 1e4 people. (d) The strong-storm wind speed loss index with an interval of 5e5 and all  
801 positive values shaded.

802 Figure 10: Analysis of CFSR precipitation rates (PR) during DJF for 1980-2010. (a) The mean  
803 precipitation during all storm activity, and (b) the mean precipitation during strong storm  
804 activity. In (a) and (b), shaded intervals are 1.0 mm day<sup>-1</sup>. (c) The difference between  
805 strong-storm precipitation and all-storm precipitation with an interval of 0.5 mm day<sup>-1</sup>.  
806 (d) The ratio (%) of strong-storm precipitation to all-storm precipitation with an interval  
807 of 10% and values exceeding 100% are shaded. (e) Percent contribution of strong storms  
808 to all-storm precipitation with an interval of 5%. For all panels, areas outside the all-  
809 storm track regions are masked out.

810 Figure 11: Analysis of CFSR intense precipitation rates (PR) in DJF for 1980-2010 in North  
811 America. (a) The percent of strong-storm days with precipitation exceeding the local 98<sup>th</sup>  
812 percentile. Shaded intervals are 1%. (b) The all-storm precipitation that exceeds the local  
813 98<sup>th</sup> percentile. Shaded intervals are 10 mm day<sup>-1</sup>. (c) As in (b) but for strong-storm pre-  
814 cipitation. (d) The difference between strong-storm precipitation and all-storm precipita-  
815 tion. Shaded intervals are 2.0 mm day<sup>-1</sup>. (e) Percent contribution of strong storms to all-  
816 storm precipitation with an interval of 5% and all values exceeding 10% shaded. Masking  
817 for all panels indicates areas where storm precipitation falls below the local 98<sup>th</sup> percen-  
818 tile.

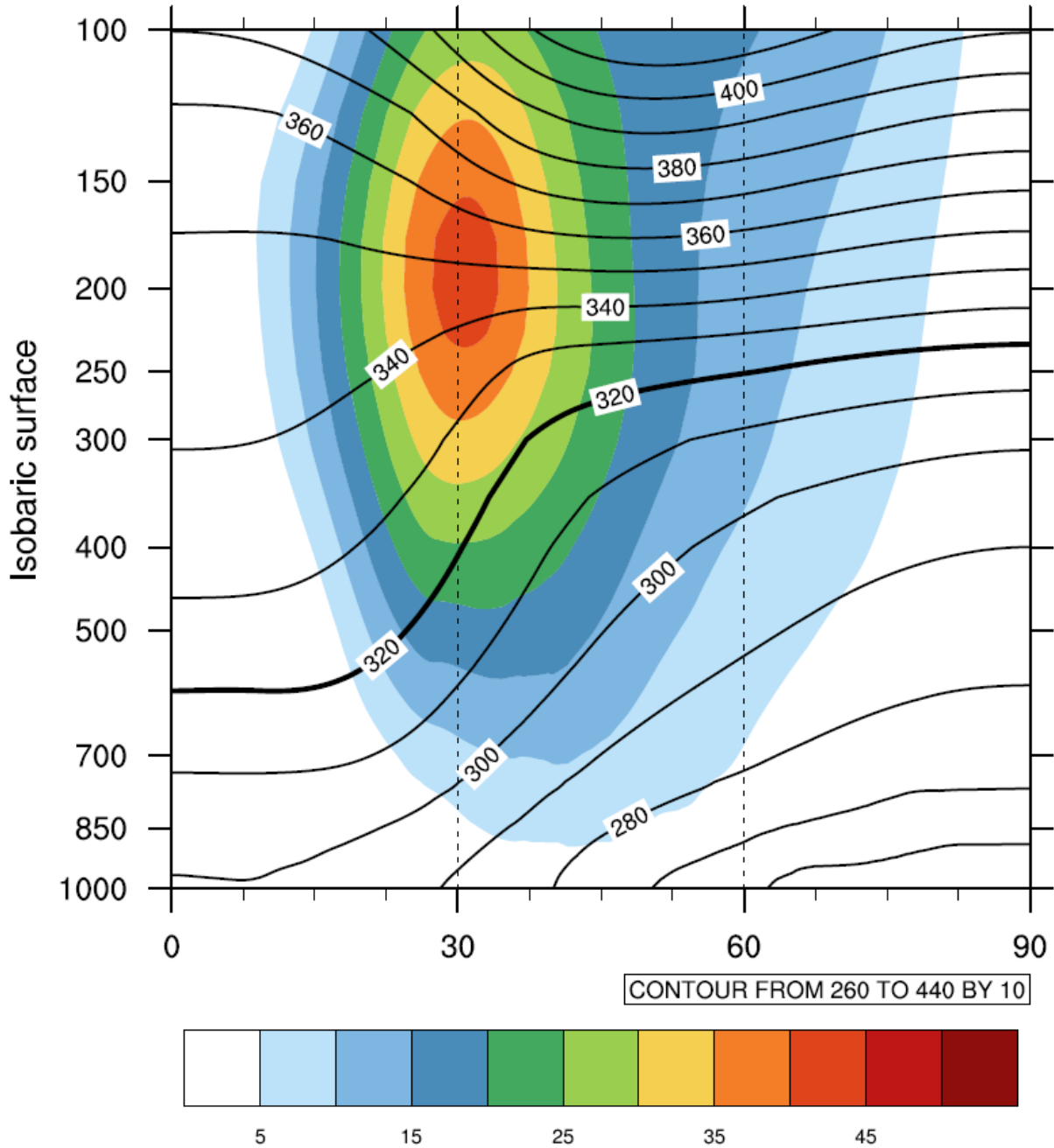
819 Figure 12: As in Fig. 10 but for GPCP precipitation for 1999-2010.

820 Figure 13: As in Figs. 11b-e but for GPCP precipitation for 1999-2010.

821

822

823



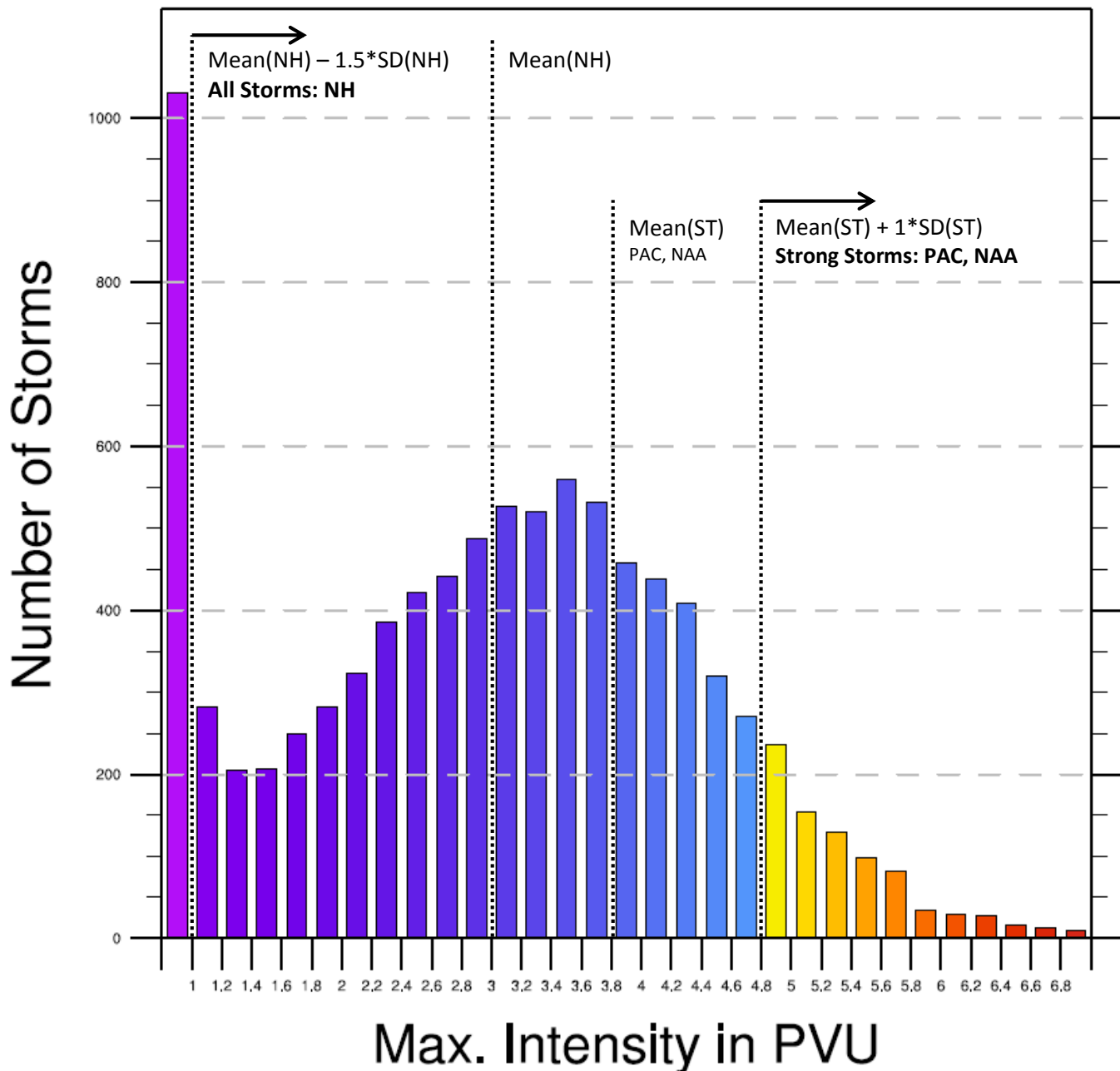
824

825

826 **Figure 1:** DJF mean zonal state in the Northern Hemisphere for 1980-2010. The mean zonal  
 827 wind is shaded with  $5.0 \text{ m s}^{-1}$  intervals. Line contours indicate the vertical distribution of mean  
 828 zonal isentropic surfaces at a  $10 \text{ K}$  contour interval. The bold black line highlights the  $\theta=320\text{K}$   
 829 surface on which the mid-latitude storm tracks are defined.

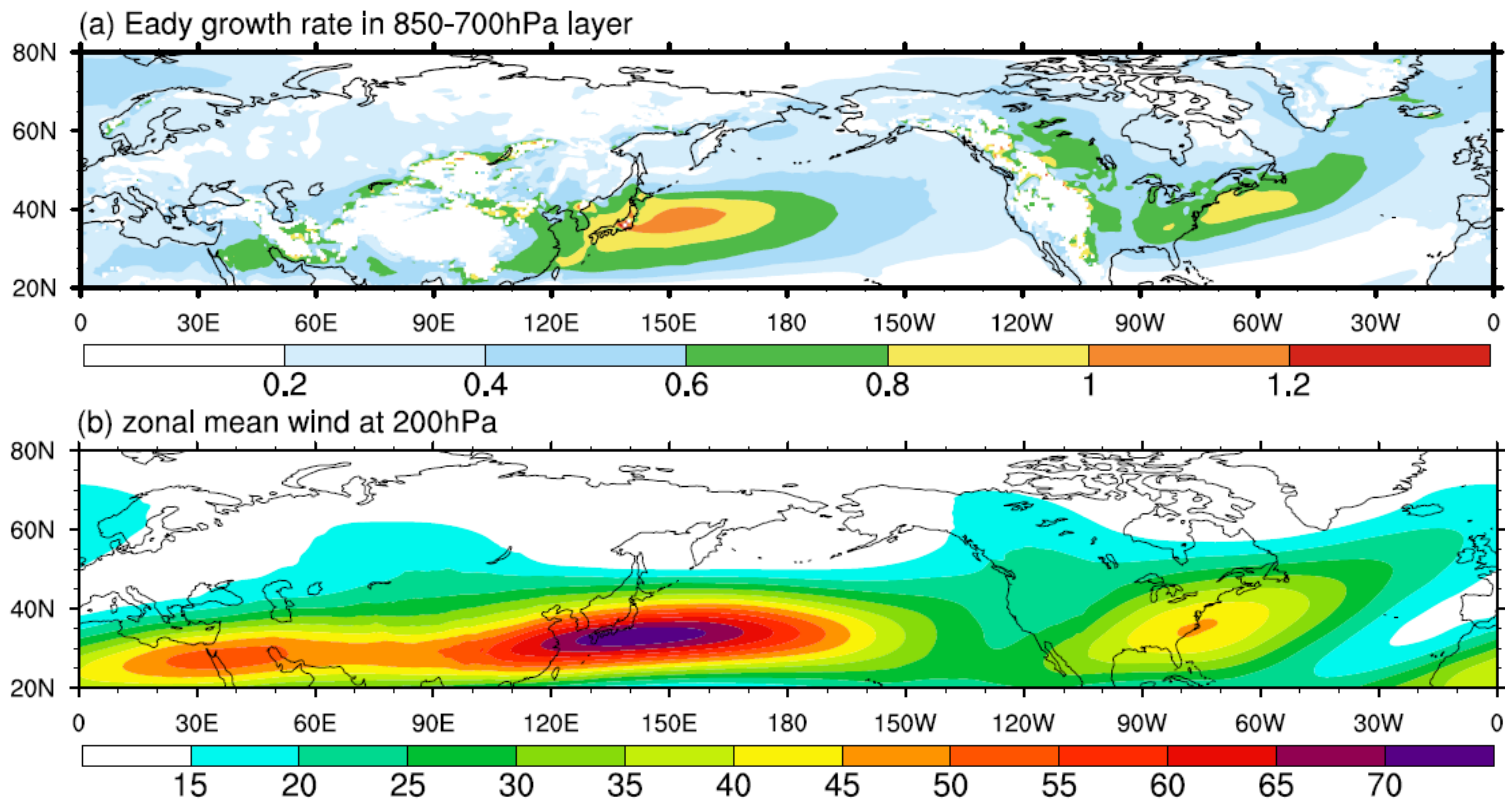
830

831



832

833 **Figure 2:** Histogram of all DJF storms binned by maximum intensity in the Northern Hemi-  
 834 sphere for 1980-2010. Maximum intensity bins are shown in the x-direction at an interval of 0.2  
 835 PVU. Storms included in the all-storm track analysis have maximum intensities of 1 PVU or  
 836 greater. Strong storms that follow the Pacific (PAC) or North American-Atlantic (NAA) storm  
 837 tracks have maximum intensities of 4.8 PVU or greater and are highlighted in warm colors. In  
 838 parentheses in the labels, NH signifies the statistics for the Northern Hemisphere, while ST indi-  
 839 cates the statistics for the PAC and NAA storm tracks.



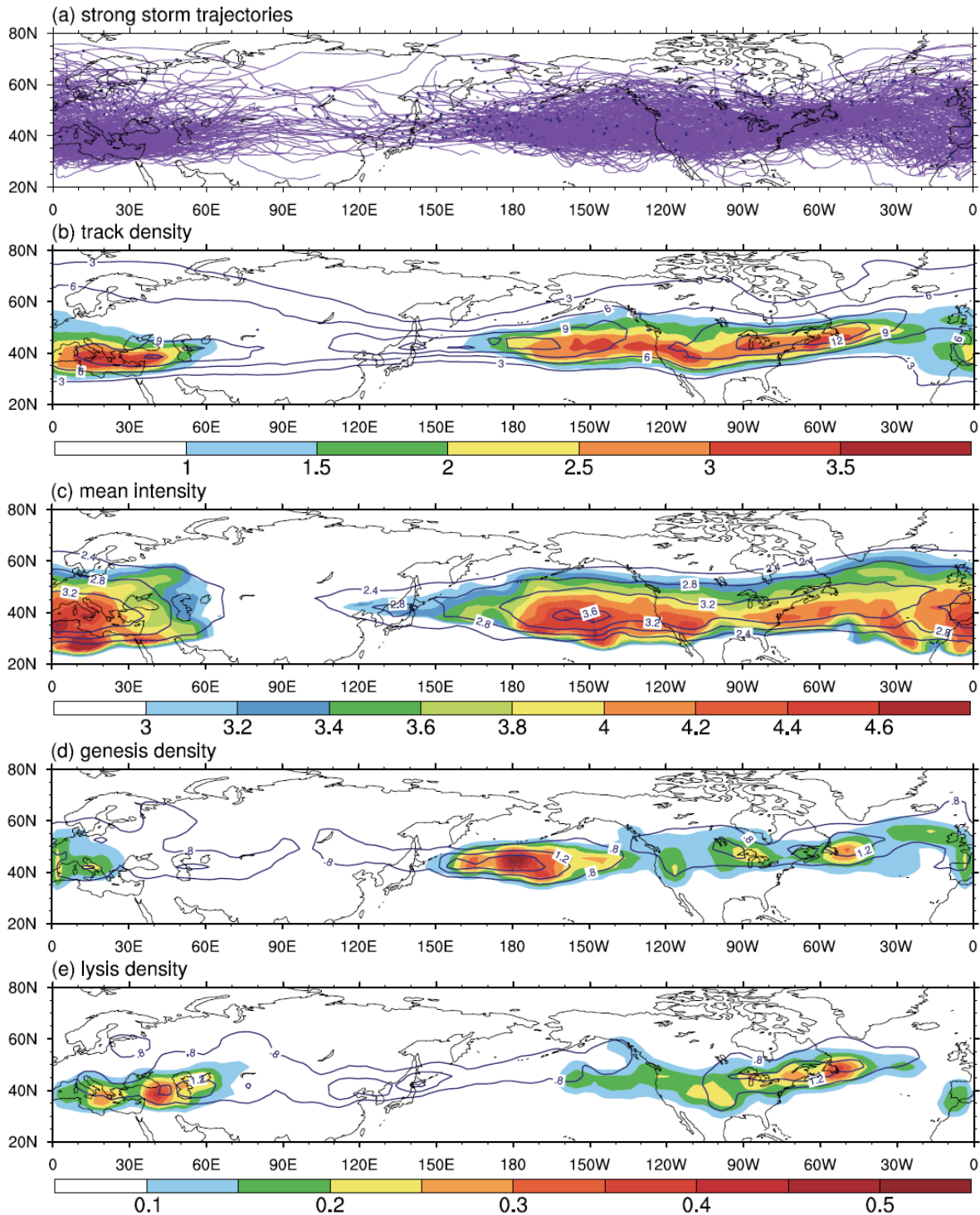
840

841 **Figure 3:** (a) 1980-2010 DJF Eady growth rate average for the 850-700 hPa layer. Values exceeding  $0.2 \text{ day}^{-1}$  are shaded at  $0.2 \text{ day}^{-1}$   
 842 intervals. Masked areas over the continents indicate regions where the land extends above the 850-hPa surface. (b) Zonal mean wind  
 843 at 200-hPa. Values exceeding  $15 \text{ m s}^{-1}$  are shaded.

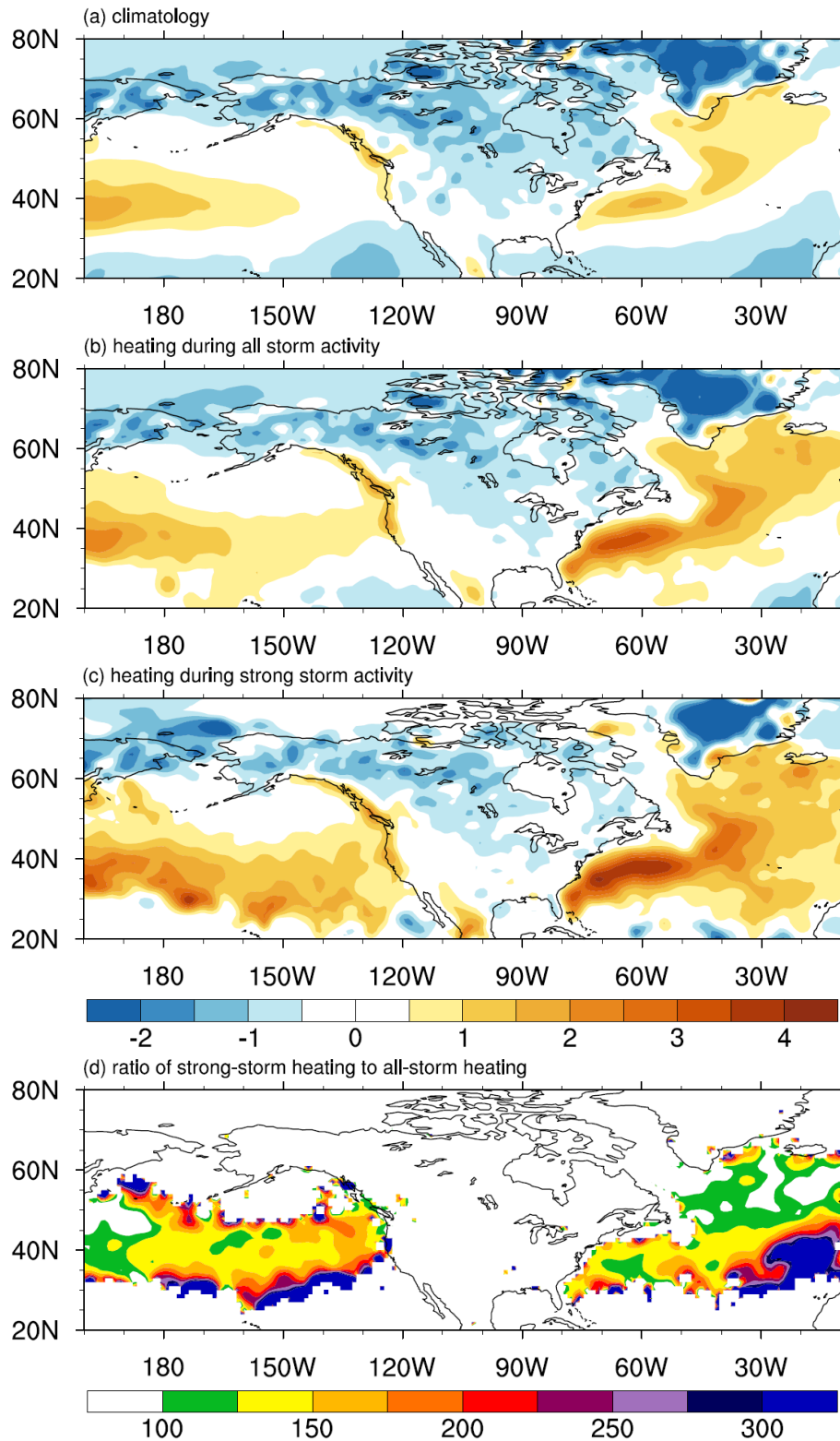
844

845

846

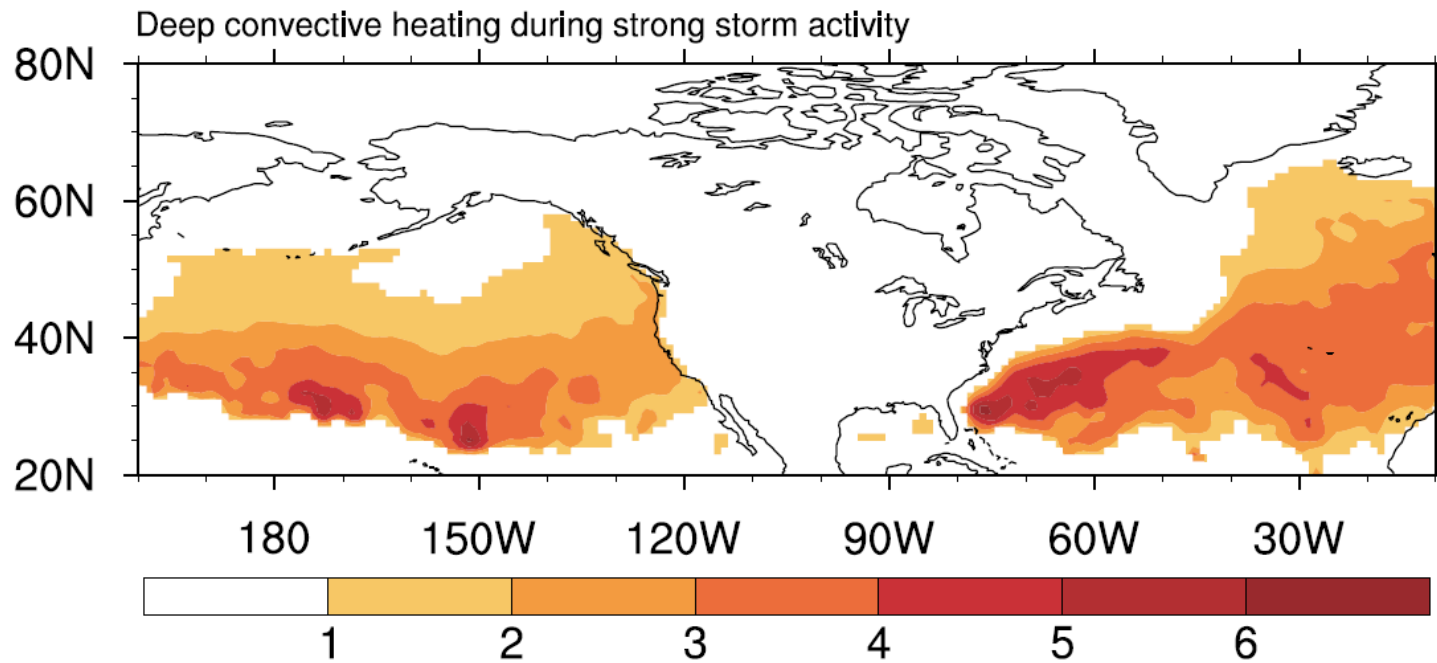


847 **Figure 4:** Storm track statistics in the Northern Hemisphere DJF season for 1980-2010. All-  
 848 all-storm tracks properties are depicted in contours, while the strong-storm track properties are  
 849 shaded. (a) Individual trajectories of strong storms; (b) Track density for all-storm tracks (con-  
 850 tours at intervals of 3.0 storms per  $10^6$  km<sup>2</sup> per month) and strong-storm tracks (shaded at inter-  
 851 vals of 0.5 storms per  $10^6$  km<sup>2</sup> per month); (c) Mean intensity of all-storm tracks (contour inter-  
 852 vals of 0.4 PVU) and strong-storm tracks (shaded at intervals of 0.2 PVU); (d) cyclogenesis den-  
 853 sity for all-storm tracks (contours at intervals of 0.4 storms per  $10^6$  km<sup>2</sup> per month) and strong-  
 854 storm tracks (shaded at intervals of 0.05 storms per  $10^6$  km<sup>2</sup> per month); (e) as (d) but for cy-  
 855 clogenesis.



856

857 **Figure 5:** DJF 1980-2010 vertically averaged 900-100 hPa diabatic heating: (a) Climatology; (b)  
 858 during all storm activity; and (c) during strong storm activity. (d) The ratio (%) of the strong-  
 859 storm diabatic heating to the all-storm diabatic heating. Shaded regions in (d) indicate areas  
 860 where the all-storm and strong-storm heating rates are positive.



861

862 **Figure 6:** Mean heating from deep convection during strong storm activity averaged between 900-100 hPa in the Northern Hemi-  
863 sphere DJF season for 1980-2010. Contour interval is 1.0 K day<sup>-1</sup>. Regions outside the all-storm track regions are masked out.

864

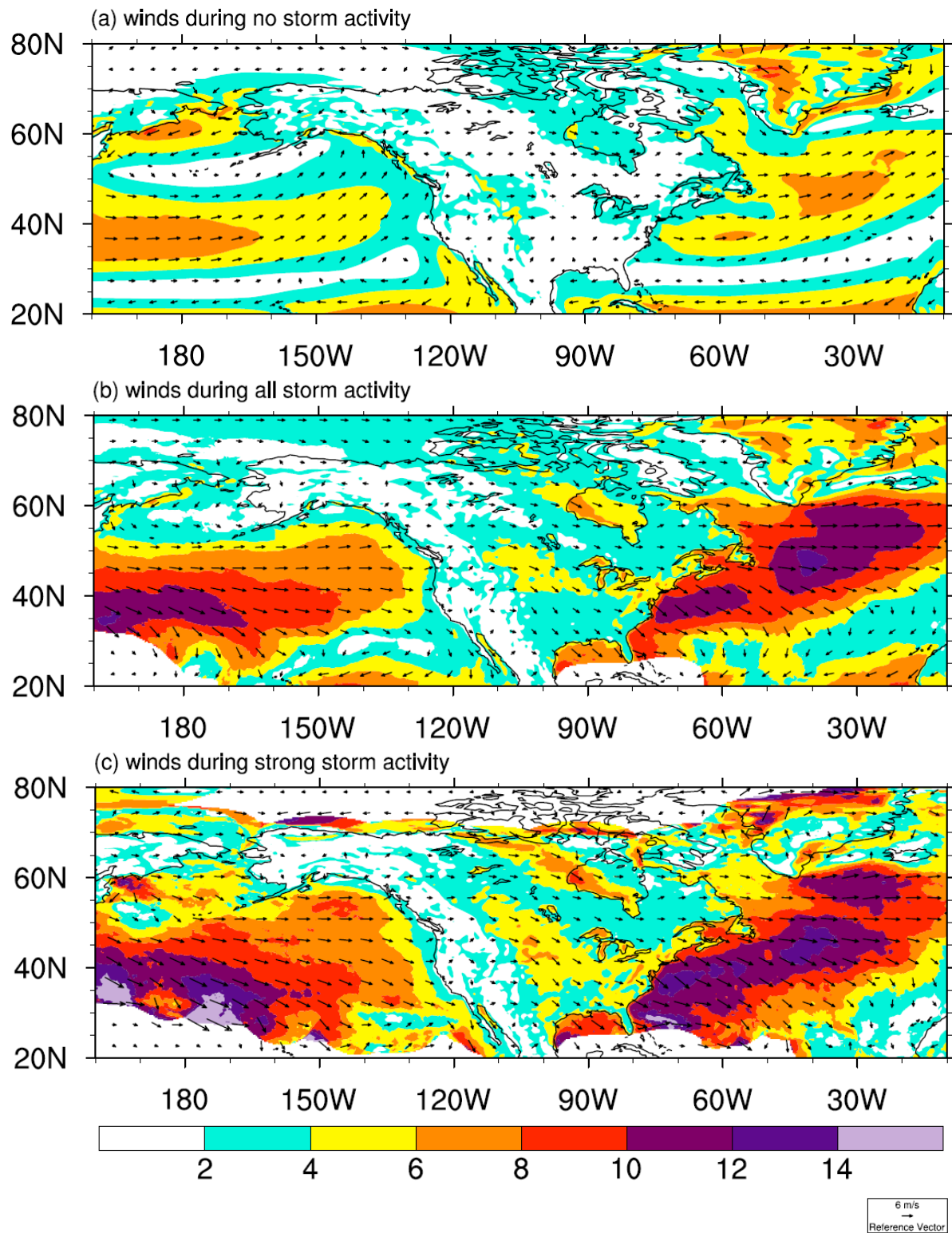
865

866

867

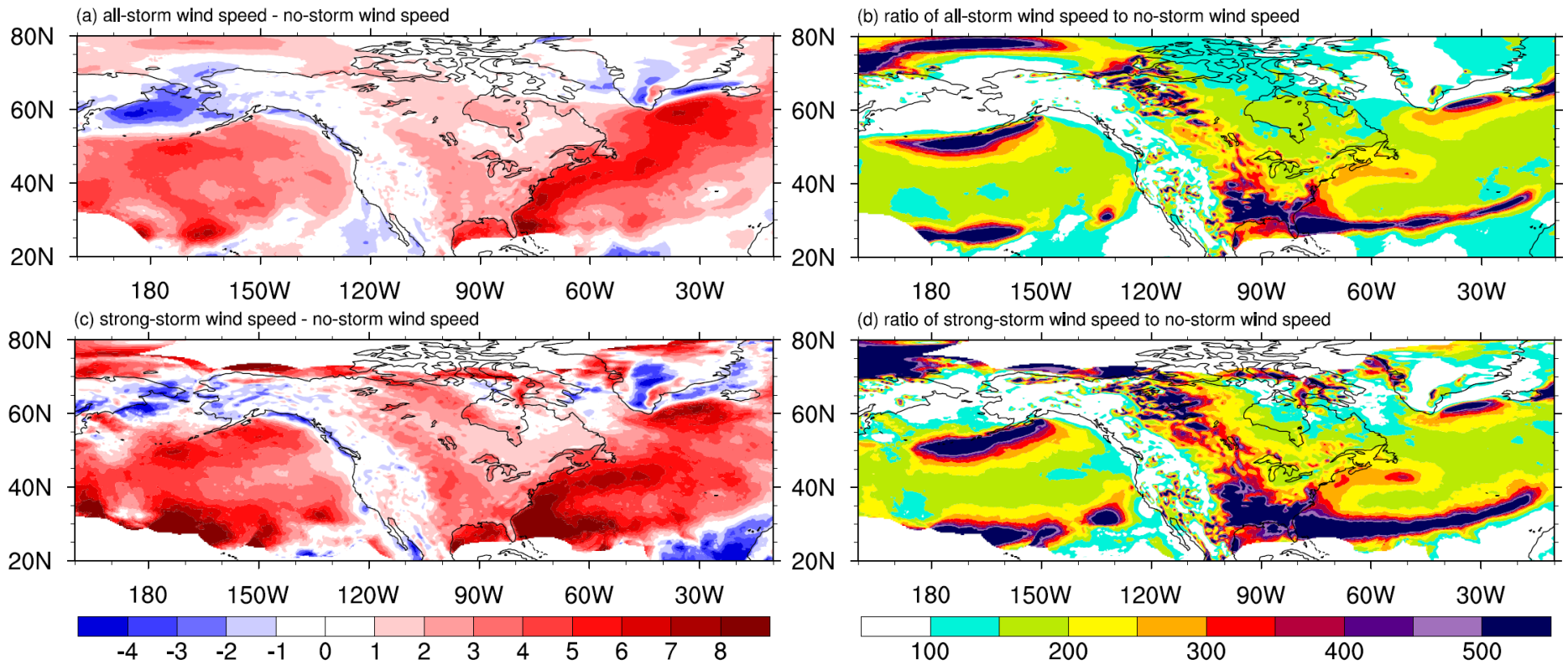
868

869



870

871 **Figure 7:** Mean near-surface wind distributions on the hybrid level 1 in DJF for 1980-2010 (a)  
 872 during no storm activity, (b) during all storm activity, and (c) during strong storm activity.  
 873 Shaded intervals are  $2.0 \text{ m s}^{-1}$ . In (b) and (c), regions outside the all-storm track regions are  
 874 masked out.



875

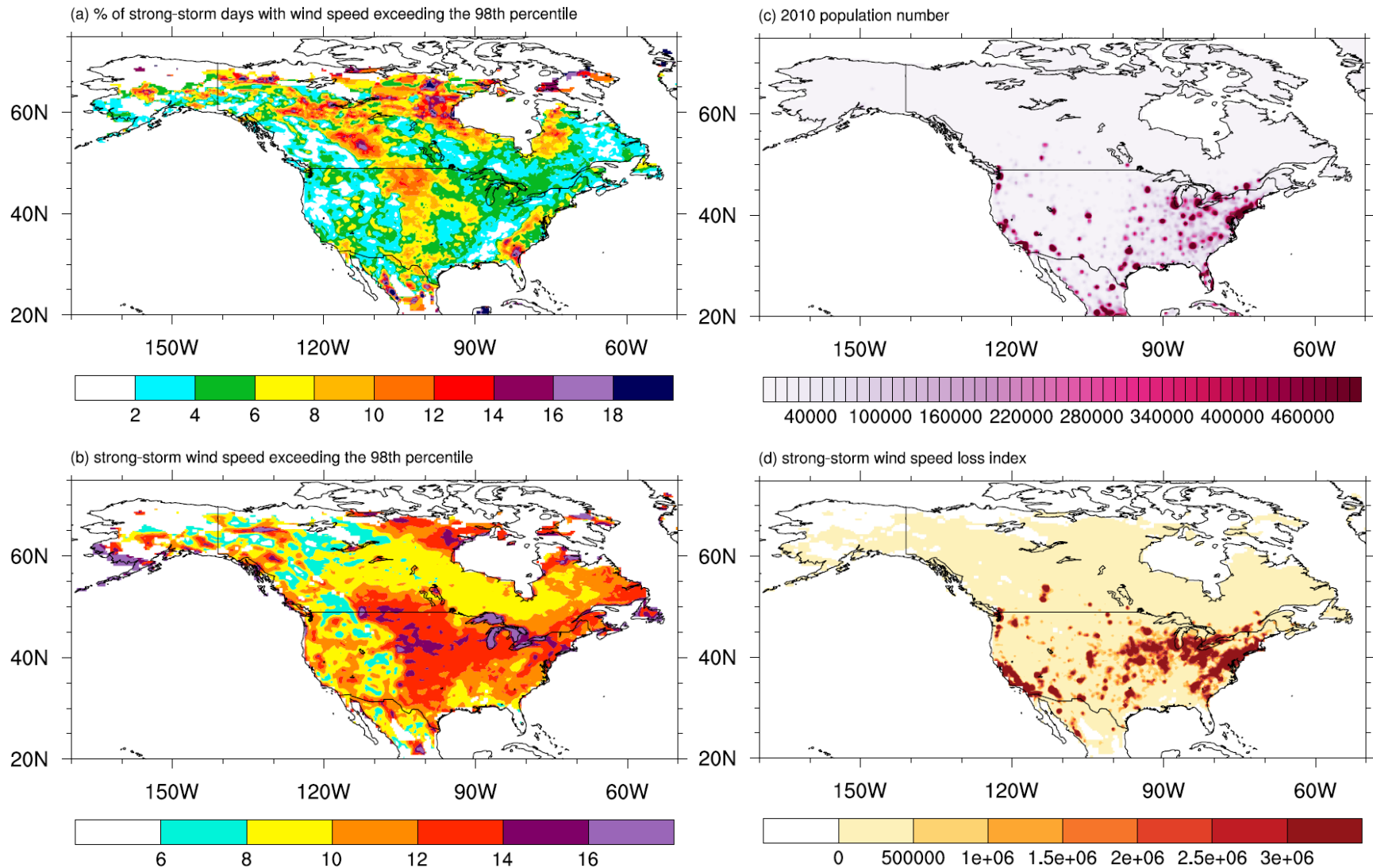
876 **Figure 8:** Wind speed comparisons based on Fig. 7. (a) Difference between all-storm wind speed and no-storm wind speed. (b) Ratio  
 877 (%) of the all-storm wind speed to the no-storm wind speed. (c) Difference between strong-storm wind speed and no-storm wind  
 878 speed. (d) Ratio (%) of strong-storm wind speed to the no-storm wind speed. In (a) and (c), shaded intervals are  $1.0 \text{ m s}^{-1}$ . In (b) and  
 879 (d), values exceeding 100% are shaded with intervals of 50%. Regions outside the all-storm track regions are masked out.

880

881

882

883



884

885 **Figure 9:** Analysis of intense near-surface wind speeds in DJF for 1980-2010 in North America. (a) Percent of strong-storm days with  
 886 wind speeds exceeding the local 98<sup>th</sup> percentile. Shaded intervals are 2%. (b) Mean strong-storm wind speeds exceeding the local 98<sup>th</sup>  
 887 percentile. Shaded intervals are 2  $\text{m s}^{-1}$ . (c) 2010 population number with an interval of 1e4 people. (d) The strong-storm wind speed  
 888 loss index with an interval of 5e5 and all positive values shaded.

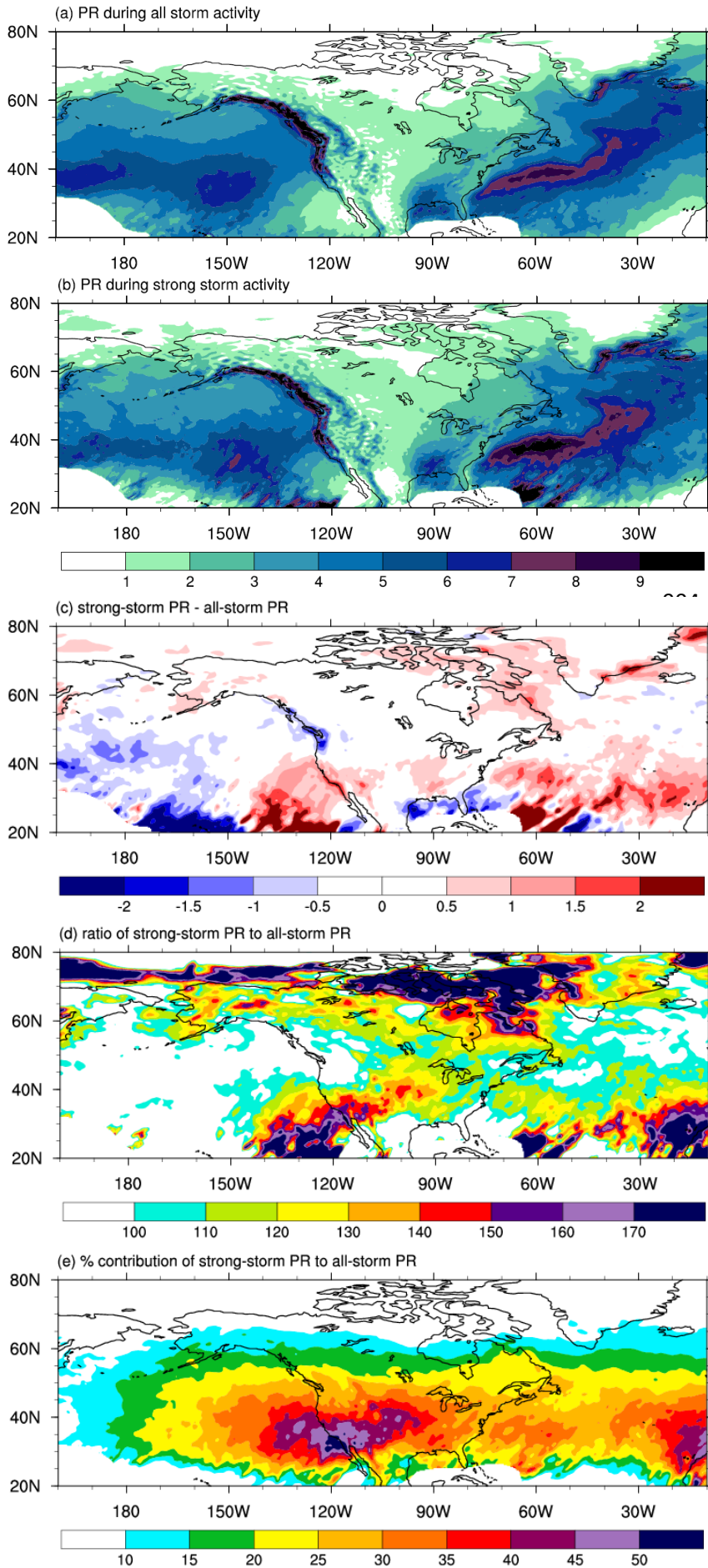


**Figure 10:** Analysis of CFSR precipitation rates (PR) during DJF for 1980-2010. (a) The mean precipitation during all storm activity, and (b) the mean precipitation during strong storm activity. In (a) and (b), shaded intervals are  $1.0 \text{ mm day}^{-1}$ . (c) The difference between strong-storm precipitation and all-storm precipitation with an interval of  $0.5 \text{ mm day}^{-1}$ . (d) The ratio (%) of strong-storm precipitation to all-storm precipitation with an interval of 10% and values exceeding 100% are shaded. (e) Percent contribution of strong storms to all-storm precipitation with an interval of 5%. For all panels, areas outside the all-storm track regions are masked out.

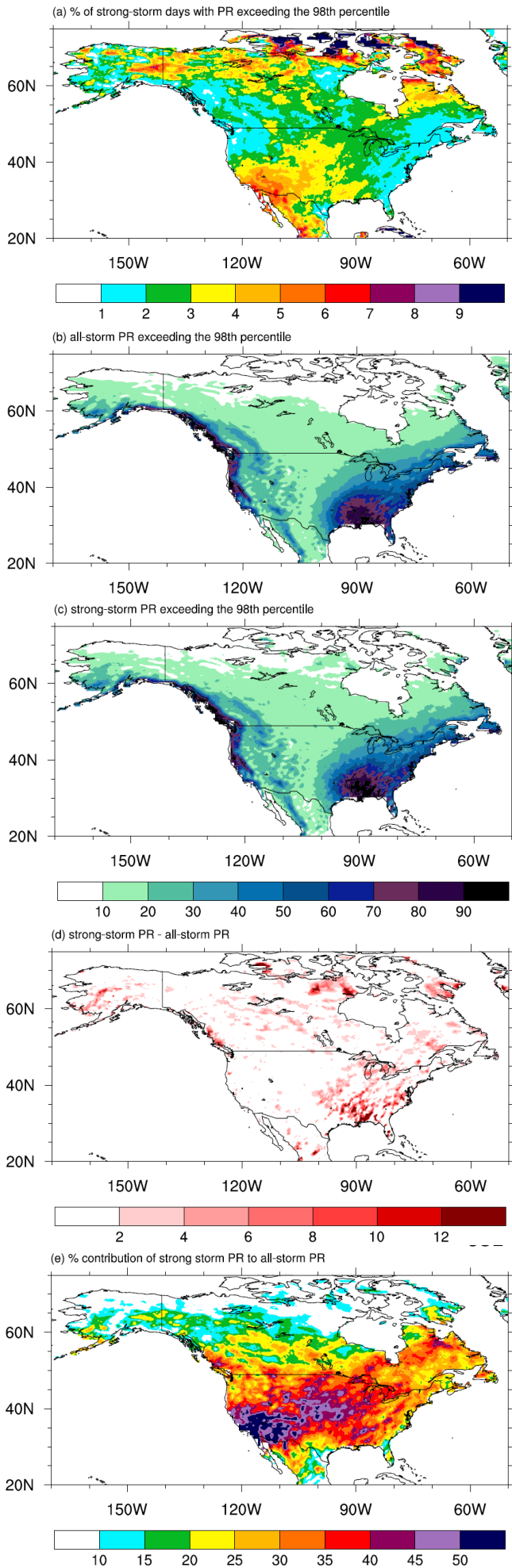


**Figure 11:** Analysis of CFSR intense precipitation rates (PR) in DJF for 1980-2010 in North America. (a) The percent of strong-storm days with precipitation exceeding the local 98<sup>th</sup> percentile. Shaded intervals are 1%. (b) The all-storm precipitation that exceeds the local 98<sup>th</sup> percentile. Shaded intervals are 10 mm day<sup>-1</sup>. (c) As in (b) but for strong-storm precipitation. (d) The difference between strong-storm precipitation and all-storm precipitation. Shaded intervals are 2.0 mm day<sup>-1</sup>. (e) Percent contribution of strong storms to all-storm precipitation with an interval of 5% and all values exceeding 10% shaded. Masking for all panels indicates areas where storm precipitation falls below the local 98<sup>th</sup> percentile.

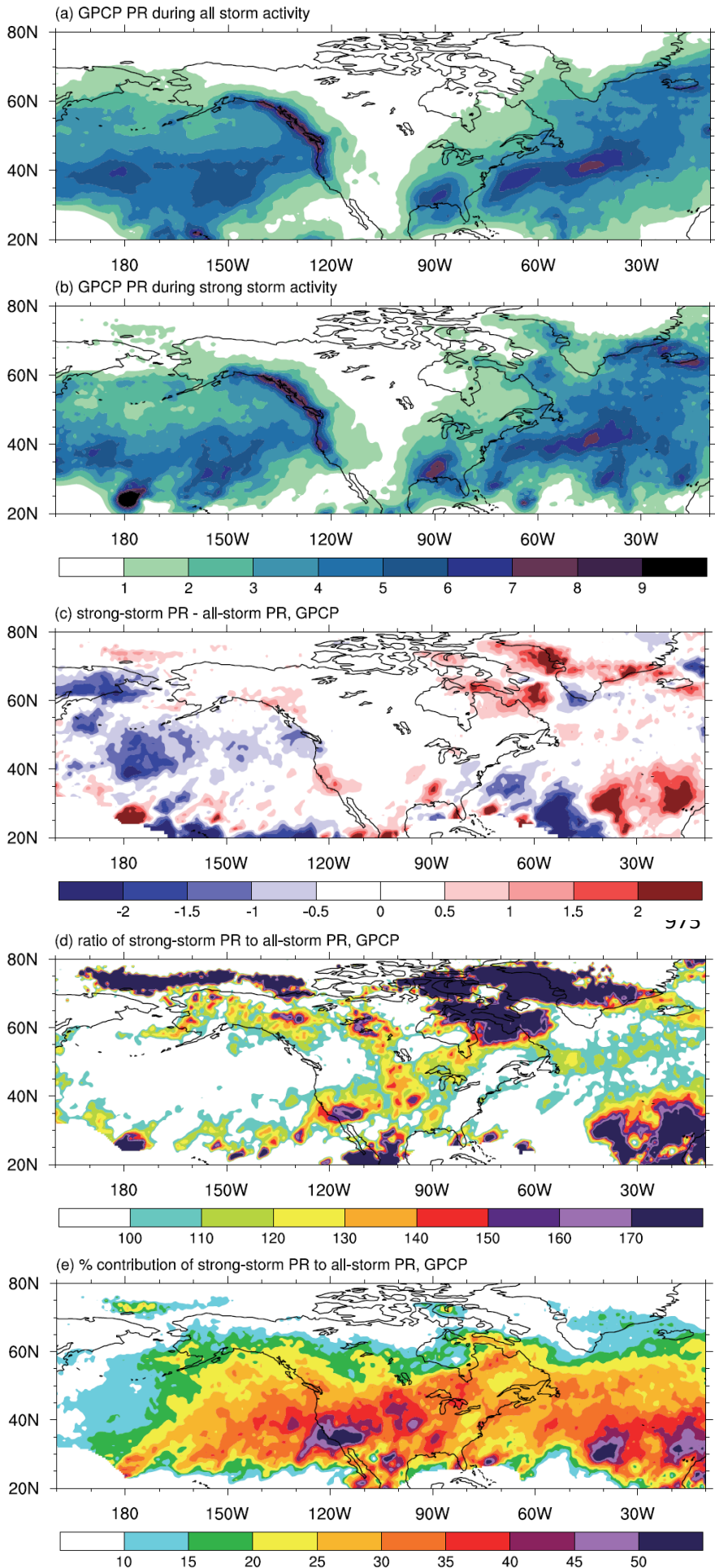


**Figure 12:** As in Fig. 10 but for GPCP precipitation for 1999-2010.

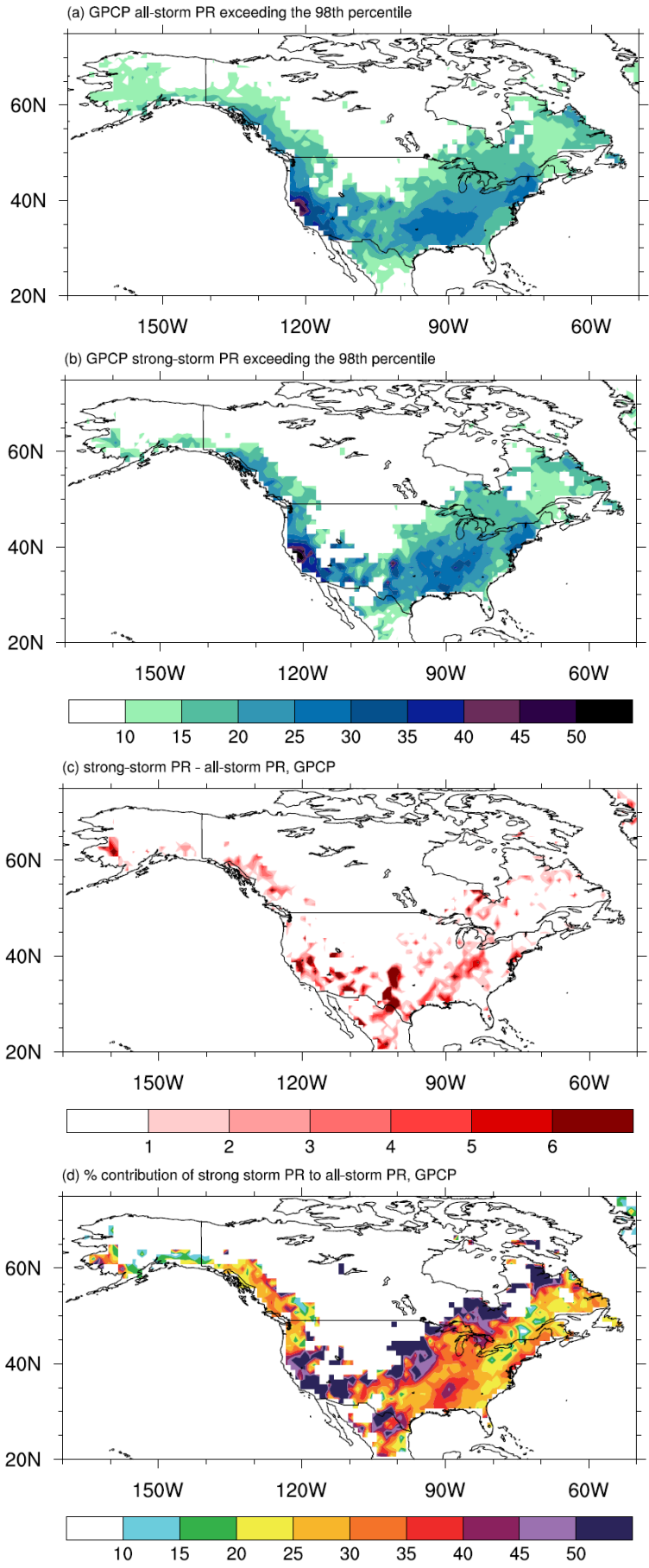


**Figure 13:** As in Figs. 11b-e but for GPCP precipitation for 1999-2010.